



HAL
open science

Impact of gradients at the martian terminator on the retrieval of ozone from SPICAM/MEx

Arianna Piccialli, Ann Carine Vandaele, Loic Trompet, Lori Neary, Sebastien Viscardy, Justin-Tyler Erwin, Anni Määttänen, Frank Daerden, Yannick Willame, Severine Robert, et al.

► **To cite this version:**

Arianna Piccialli, Ann Carine Vandaele, Loic Trompet, Lori Neary, Sebastien Viscardy, et al.. Impact of gradients at the martian terminator on the retrieval of ozone from SPICAM/MEx. *Icarus*, 2021, 353 (January), pp.art. 113598. <10.1016/j.icarus.2019.113598>. <insu-02422316>

HAL Id: insu-02422316

<https://insu.hal.science/insu-02422316v1>

Submitted on 18 Nov 2020

HAL is a multi-disciplinary open access archive for the deposit and dissemination of scientific research documents, whether they are published or not. The documents may come from teaching and research institutions in France or abroad, or from public or private research centers.

L'archive ouverte pluridisciplinaire **HAL**, est destinée au dépôt et à la diffusion de documents scientifiques de niveau recherche, publiés ou non, émanant des établissements d'enseignement et de recherche français ou étrangers, des laboratoires publics ou privés.

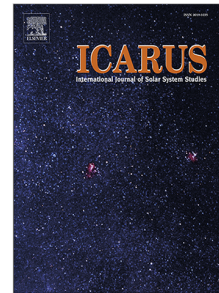


HAL Authorization

Journal Pre-proof

Impact of gradients at the Martian terminator on the retrieval of ozone from SPICAM/MEx

A. Piccialli, A.C. Vandaele, L. Trompet, L. Neary, S. Viscardy, J.T. Erwin, A. Määttänen, F. Daerden, Y. Willame, S. Robert, S. Aoki, V. Wilquet, F. Lefèvre, F. Montmessin



PII: S0019-1035(19)30292-1
DOI: <https://doi.org/10.1016/j.icarus.2019.113598>
Reference: YICAR 113598

To appear in: *Icarus*

Received date : 22 April 2019
Revised date : 22 October 2019
Accepted date : 6 December 2019

Please cite this article as: A. Piccialli, A.C. Vandaele, L. Trompet et al., Impact of gradients at the Martian terminator on the retrieval of ozone from SPICAM/MEx. *Icarus* (2019), doi: <https://doi.org/10.1016/j.icarus.2019.113598>.

This is a PDF file of an article that has undergone enhancements after acceptance, such as the addition of a cover page and metadata, and formatting for readability, but it is not yet the definitive version of record. This version will undergo additional copyediting, typesetting and review before it is published in its final form, but we are providing this version to give early visibility of the article. Please note that, during the production process, errors may be discovered which could affect the content, and all legal disclaimers that apply to the journal pertain.

© 2019 Published by Elsevier Inc.

Impact of gradients at the Martian terminator on the retrieval of ozone from SPICAM/MEx

A. Piccialli^{a,*}, A. C. Vandaele^a, L. Trompet^a, L. Neary^a, S. Viscardy^a, J.T. Erwin^a, A. Määttänen^b, F. Daerden^a, Y. Willame^a, S. Robert^a, S. Aoki^a, V. Wilquet^a, F. Lefèvre^b, F. Montmessin^c

^aPlanetary Aeronomy, Royal Belgian Institute for Space Aeronomy, 3 av. Circulaire, B-1180 Brussels, Belgium

^bLATMOS/IPSL, Sorbonne Université, UVSQ, CNRS, Paris, France

^cLATMOS/IPSL, UVSQ Université Paris-Saclay, Sorbonne université, CNRS, Guyancourt, France

Abstract

Rapid variations of pressure, temperature and illumination at the day-night terminator have the potential to cause asymmetries in the abundance distribution of the atmosphere constituents along the line of sight (LOS) of a solar occultation experiment. Ozone, in particular, displays steep density gradients across the terminator of Mars due to photolysis. Nowadays, most of the retrieval algorithms for solar and stellar occultations rely on the assumption of a spherically symmetrical atmosphere. However, photochemically induced variations near sunrise/sunset conditions need to be taken into account in the retrieval technique in order to prevent inaccuracies.

We investigated the impact of gradients along the LOS of the solar occultation experiment SPICAM/Mars Express for the retrieval of ozone under sunrise/sunset conditions. In order to test the impact of different gradients, we selected four occultations at sunrise and at sunset each. Sunset occultations are located near the equator, while sunrise observations are situated at high latitudes in the South, because of the geometry of the orbit.

We used the diurnal variations in the ozone concentration obtained from a three-dimensional General Circulation Model (GEM-Mars) together with an adapted radiative transfer code (ASIMUT). The General Circulation Model (GCM) suggests that ozone variations strongly depend on latitude,

*Corresponding author

Email addresses: arianna.piccialli@aeronomie.be (A. Piccialli), A-C.Vandaele@aeronomie.be (A. C. Vandaele), Loic.Trompet@aeronomie.be (L. Trompet), Lori.Neary@aeronomie.be (L. Neary), Sebastien.Viscardy@aeronomie.be (S. Viscardy), justin-tyler.erwin@aeronomie.be (J.T. Erwin), anni.maattanen@latmos.ipsl.fr (A. Määttänen), Frank.Daerden@aeronomie.be (F. Daerden), yannick.willame@aeronomie.be (Y. Willame), Severine.Robert@aeronomie.be (S. Robert), Shohei.Aoki@aeronomie.be (S. Aoki), Valerie.Wilquet@aeronomie.be (V. Wilquet), franck.lefevre@latmos.ipsl.fr (F. Lefèvre), franck.montmessin@latmos.ipsl.fr (F. Montmessin)

altitude, and season. As shown by the model, near the equator and below 25 km, ozone changes only slightly with local time. Around 45 km, the density changes by several orders of magnitude across the terminator. At high latitudes in the South, during northern winter time, ozone variations at the terminator are negligible.

The impact of gradients on ozone retrievals is strongly related to the local atmospheric structure as predicted by the GCM. Sunset ozone retrievals are smaller than retrievals obtained assuming a spherically symmetrical atmosphere, with a maximum change of about 20%. At sunrise, the impact of gradients on the retrievals is negligible. This behavior can be explained by the specific geometry of sunrise observations, all situated at high latitudes in the South.

Keywords: Mars, atmosphere, Occultations, Ultraviolet observations, Radiative transfer, Photochemistry

1. Introduction

Occultation, both solar and stellar, is a powerful technique to measure the vertical distribution of trace gases in planetary atmospheres. The major advantages of this technique are its high vertical resolution and its self-calibration mode. While stellar occultations probe the atmosphere preferably at night time, solar occultation are restricted to the terminator (Bertaux et al., 2006).

The atmosphere of a terrestrial planet at the day-night terminator is a region of great interest characterized by gradients of density and temperature, driven by differences in the solar illumination, and by sharp transitions in the chemical regime. Rapid variations in species concentration at the terminator have the potential to cause asymmetries in the species distributions along the line of sight (LOS) of a solar occultation experiment. Ozone, in particular, displays rapid changes due to photolysis more pronounced on the day side than on the night side (Natarajan et al., 2005; Lefèvre et al., 2004). Nowadays, most of the retrieval algorithms for solar and stellar occultations rely on the assumption of a spherically symmetrical atmosphere (Vandaele et al., 2006; Quémerais et al., 2006). However, photochemically induced variations near sunrise/sunset conditions need to be taken into account in the retrieval process in order to prevent inaccuracies (Boughner et al., 1980; Natarajan et al., 2005). In order to handle concentration gradients along the line of sight it is necessary to improve the retrieval schemes used to analyze occultation observations.

In the present paper, we test an improved retrieval scheme that handles different gradients along the line of sight and we focus in particular on the retrieval of ozone from SPICAM/Mars

20 Express solar occultations taking into account variations in the temperature and in the ozone
21 concentration at the day/night terminator. Ozone is a species with a short chemical lifetime and
22 characterized by sharp gradients at the day-night terminator both on Earth and on Mars. On Mars,
23 3D General Circulation Models (GCMs) predict the existence of two ozone layers (Lefèvre et al.,
24 2004; Daerden et al., 2019), instead of just one layer as on Earth. This was confirmed by SPICAM
25 stellar occultations (Lebonnois et al., 2006), which revealed their existence on the nightside. The
26 first layer is located below 30 km, and the second one - seasonally and spatially variable - is situated
27 at higher altitudes between 30 and 60 km. While the lower layer displays only a weak diurnal cycle,
28 the upper layer is strongly depleted by ultraviolet radiation at sunrise. It reappears as the Sun sets
29 due to the recombination of O and O₂.

30 Previous observations reported that the largest ozone quantities are observed at high latitudes
31 in the winter hemisphere where water vapour has condensed on the polar cap (Lebonnois et al.,
32 2006; Willame et al., 2017). This was expected since ozone is anti-correlated to water vapour.
33 Lower quantities of ozone are found at low latitudes and in the summer hemisphere (Lefèvre et al.,
34 2004; Daerden et al., 2019).

35 We briefly describe the SPICAM-UV solar occultation dataset in Section 2. The GCM used as
36 an input for this study is presented in Section 3. We review the retrieval technique in Section 4
37 and then present the results in Sections 5–7.

38 **2. SPICAM-UV solar occultation dataset**

39 SPICAM (SPectroscopie pour l'Investigation des Caractéristiques Atmosphériques de Mars), on
40 board the ESA's mission Mars Express, is a remote sensing spectrometer observing in the ultraviolet
41 (118 – 320 nm) and in the near infrared (1 – 1.7 μ m). A detailed description of the instrument
42 as well as its scientific objectives can be found in Bertaux et al. (2006). In the solar occultation
43 mode, the UV instrument is used to measure the vertical profiles of O₃ and aerosols of the Martian
44 atmosphere (Määttä et al., 2013). During a solar occultation, the instrument points through
45 the atmosphere toward the Sun as it rises or sets. When the instrument's line of sight to the Sun
46 intersects the atmosphere, the solar light is absorbed by the atmospheric constituents (Quémerais
47 et al., 2006; Montmessin et al., 2006; Forget et al., 2009; Lebonnois et al., 2006). A reference solar
48 spectrum is obtained by recording the solar light above the dense part of the atmosphere (above

Table 1: Solar occultations analysed in this study. The reference location for each profile is determined at the surface. Ls is the solar longitude.

Occultation	Longitude	Latitude	Ls	Local time	Terminator
00472A02	342.76	-9.23	42.37	17.82	Sunset
00584A02	143.05	-18.02	56.27	17.52	Sunset
00633A02	10.80	-21.67	62.29	17.37	Sunset
00655A01	10.25	-23.46	64.99	17.30	Sunset
00584A03	47.56	-68.94	56.28	11.44	Sunrise
00633A03	280.26	-67.62	62.30	11.59	Sunrise
00642A02	117.83	-67.42	63.40	11.65	Sunrise
00682A02	157.93	-66.46	68.30	12.05	Sunrise

49 120 km). The ultraviolet sensor of SPICAM has a spectral resolution of 0.51 nm. The vertical
50 sampling resolution obtained in solar occultation is less than 1 km.

51 Figure 1 displays transmission spectra obtained at different altitudes for the observation 00633A02.
52 The signal below 200 nm has a poor signal-to-noise ratio (SNR) due to the low emission of the Sun
53 at those wavelengths and is not used in the retrievals. The ozone absorption band (Hartley band)
54 is clearly visible around 250 nm. The aerosols affect the entire spectral range by attenuating the
55 spectrum approximately uniformly (Montmessin et al., 2006).

56 The reference location for each occultation is determined at the surface (see Figure 2). However,
57 the relative motion of the source often means that the locus of tangent points is far from vertical,
58 leading to 'slanted' profiles, extending over several hundred kilometers horizontally. A solar occul-
59 tation profile is then spread over a latitude and longitude interval, usually smaller than 20° . The
60 local time of the tangent point is also changing at each altitude during an occultation. The spread
61 of the occultation profile is larger close to the poles and decreases approaching the equator.

62 For this study we analyzed data from eight solar occultations acquired by SPICAM-UV between
63 June and August 2004 (MY27) both at sunrise and at sunset (see Table 1). We selected only occul-
64 tations acquired before June 2005 in order to avoid the oscillations caused by the MARSIS/MEx
65 antenna (Määttä et al., 2013). Due to such a constraint, there is a clear bias in the geolocaliza-
66 tion of sunrise and sunset occultations: all sunset occultations are located near the equator while
67 sunrise occultations are situated at high latitudes.

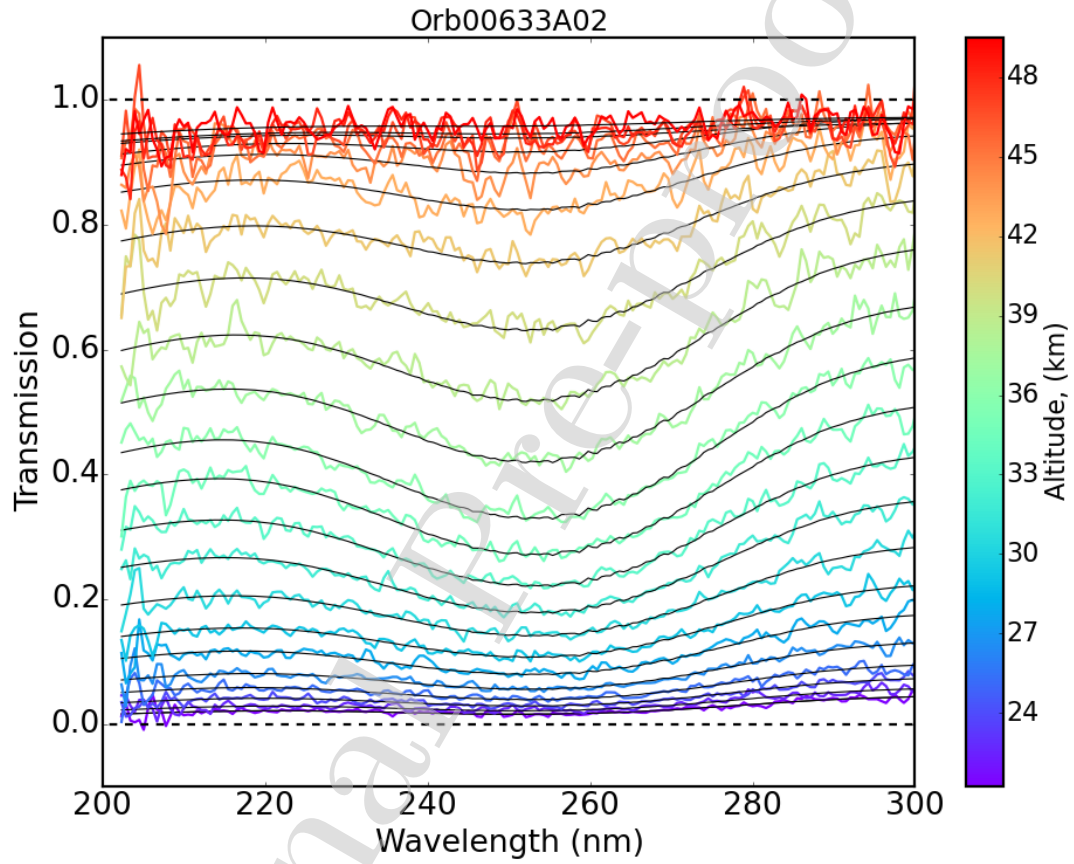


Figure 1: Example of SPICAM transmission spectra at different altitudes: (blue) low altitudes; (red) high altitudes. Black lines are fitted spectra calculated using the radiative transfer code ASIMUT.

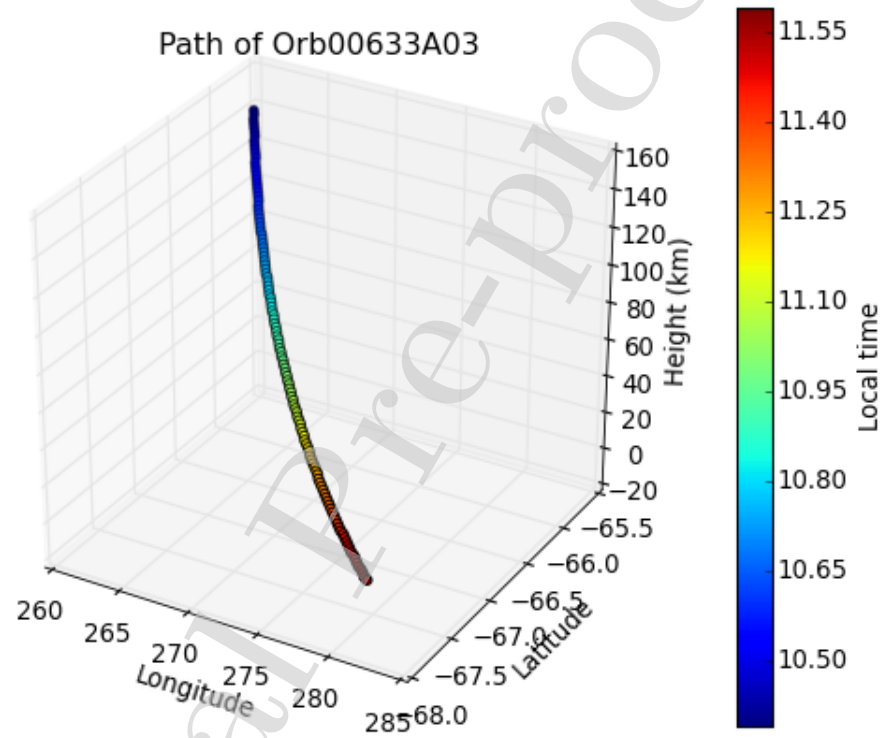


Figure 2: Example of path described by the tangent point during an occultation (#00633A03). The colorbar shows the local time (hr) variation along the path.

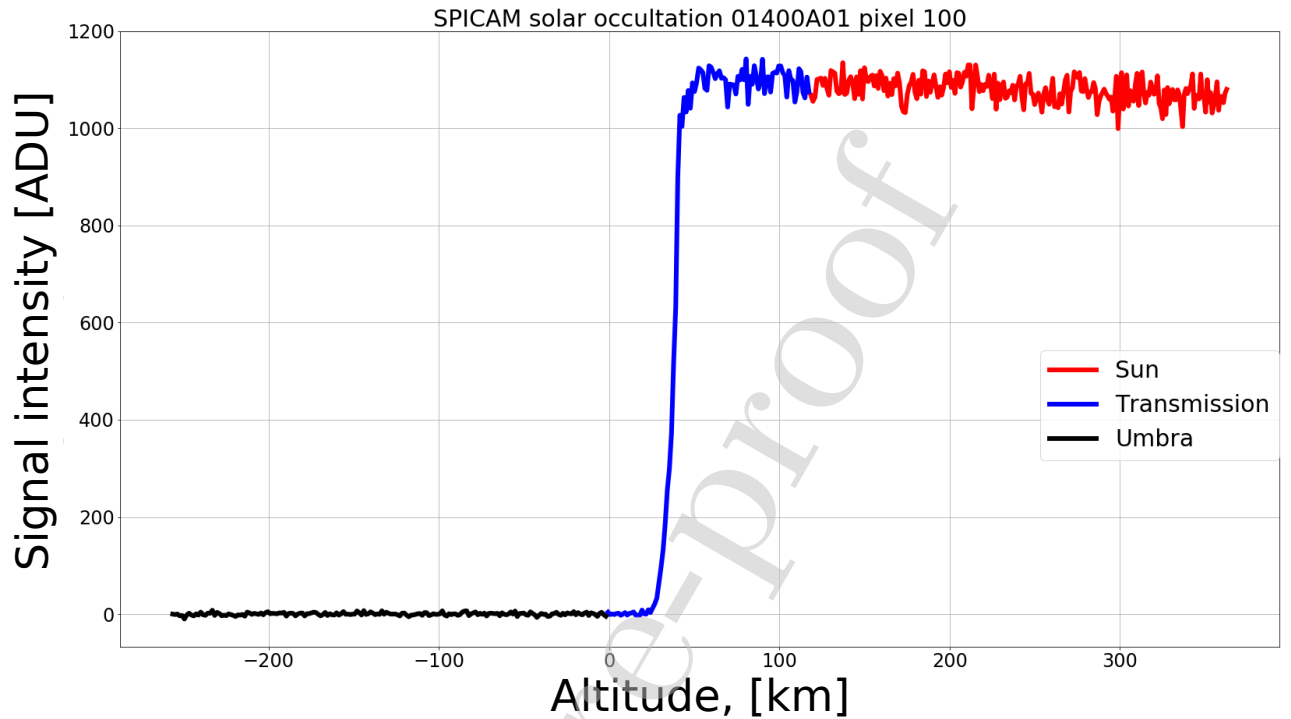


Figure 3: Example of intensity of the signal recorded on one pixel of the detector. The "Sun" region lies above 120 km (red), the "Transmission" region between 0 and 120 km (blue) and the "Umbra" region under about 15 km of tangent altitude (black).

68 2.1. Transmittance estimation

69 The spectra recorded during a solar occultation measurement can be separated in three regions
70 represented on Figure 3:

- 71 • The "Sun" region: it contains solar spectra recorded when the LOS does not cross the atmo-
72 sphere,
- 73 • The "Transmission" region: it contains atmospheric spectra recorded when the LOS crosses
74 the atmosphere,
- 75 • The "Umbra" region: it contains the data recorded when all the light of the Sun has been
76 absorbed or occulted by Mars.

77 For the Martian atmosphere, and given the SNR of SPICAM-UV, we consider that the separation
 78 between the "Sun" and the "Transmission" region occurs at 120 km of tangent altitude.

79 The solar reference spectrum S is computed by extrapolating, for each pixel, the intensity of
 80 the spectra recorded in the "Sun" region using a linear regression. Transmittances Tr are, then,
 81 computed by dividing the spectra of the "Transmission" region by the extrapolated solar reference
 82 spectrum S at the same time, i.e. at the same tangent altitude (in occultation measurements, each
 83 spectrum has a particular time of measurement and tangent altitude and they are proportional
 84 or inversely proportional for egress or ingress measurement, respectively). The noise δTr on the
 85 transmittances is calculated using the formula from Vandaele et al. (2013), and the SNR is the ratio
 86 of the transmittance Tr to the corresponding noise δTr :

$$\delta P(t) = \delta U + \sqrt{Tr(t)}(\delta S - \delta U) \quad (1a)$$

$$\delta Tr(t) = \frac{\sqrt{\delta P(t)^2 + Tr(t)^2 \delta S^2}}{S(t)} \quad (1b)$$

$$SNR(t) = \frac{Tr(t)}{\delta Tr(t)} \quad (1c)$$

87 where δS and δU are the noise in the "Sun" region and in the "Umbra" region respectively. They
 88 are computed for each pixel by taking the standard deviation of the signal in the corresponding
 89 region. δP is the noise for the "Transmission" region in unit of ADU (Analog-to-Digital units).

90 In a perfect measurement, the LOS of the instrument does not move on the Sun, and the detector
 91 sensitivity remains constant, so that we would expect the signal to be constant in the "Sun" region
 92 within the noise. In practice, this is not always the case, and taking into account all the spectra
 93 recorded in the "Sun" region may not lead to the correct extrapolated solar spectra. To take into
 94 account a variation of the signal along the occultation, we use a simple linear regression on the
 95 signal of each pixel in the Sun region, in order to extrapolate a solar reference spectrum for each
 96 spectrum in the transmission region.

97 We have adapted the algorithm used for SOIR (Nevejans et al., 2006) on Venus Express and
 98 described in Trompet et al. (2016). This algorithm is based on the fact that we expect that the
 99 transmittances Tr will not deviate too much from 1.0 for the highest tangent altitudes, i.e. when
 100 the solar light is still too weakly absorbed to be seen on the spectra. Concretely, we expect that
 101 the estimated transmittances do not deviate further than n times the values of the noise δTr :

102 $Tr - n * \delta Tr < 1 < Tr + n * \delta Tr$, where n is in the range [1, 3].

103 The value n is not fixed and a loop over that value has been added as the dataset can be rapidly
 104 treated. The value n begins with the value of 1 and increases by step of 0.5 if the criteria (Eq. 1c)
 105 are not satisfied until the value of 3.

106 During the acquisition of a spectrum, the signal is spread on several spatial lines of the detector.
 107 For SPICAM, the signal on these different lines are binned into five bands.

108 For this study, these five bands have been added up to enhance the SNR ratio of the calibrated
 109 spectra. Using the five bands, we noticed an increase of the mean SNR over the whole dataset of
 110 30% with respect to the case where only the three middle bands were taken and of 67% with respect
 111 to the case where only the middle band was used.

112 3. Model fields of atmospheric quantities

113 We use the GEM-Mars three-dimensional General Circulation Model (GEM-Mars GCM) with
 114 online chemistry (meaning photolysis and reaction rates, production and loss rates are computed
 115 at each model integration step) for the atmospheric input profiles and to quantify the gradients
 116 across the terminator. The model includes gas-phase photochemistry (46 reactions in total), pa-
 117 rameterizations for molecular diffusion, CO₂ condensation/sublimation and pressure cycle, water
 118 cycle with cloud radiative feedbacks, non-condensable gas enrichment, and a dust lifting scheme for
 119 saltation and dust devils. The gas-phase species, dust and water ice particles are advected using
 120 the semi-Lagrangian dynamical core.

121 The photolysis and reaction rates are calculated at each model integration time step, and ab-
 122 sorption by CO₂, O₂, O₃, H₂O and H₂O₂ along the line of sight as well as attenuation by dust and
 123 water ice are taken into account.

124 A detailed description and evaluation of the model can be found in Neary and Daerden (2018)
 125 with further information regarding the chemistry in Daerden et al. (2019).

126 To provide input profiles, the model was run at a horizontal resolution of $4^\circ \times 4^\circ$ (approximately
 127 237 km longitudinal spacing at the equator) and 103 unevenly spaced vertical levels from the surface
 128 up to ~ 150 km. The spacing of levels near the surface is of the order of meters, increasing to ~ 1
 129 km in the 10 – 50 km altitude range. A simulation was performed for a generic Mars year with
 130 average dust loading (not year specific) resulting from the dust-lifting scheme in the model with

131 orbital parameters set to MY 28. The dynamical and chemical integration timestep was 1/48th of
132 a Mars sol (~ 30 minutes).

133 For the gradients, profiles of temperature and ozone were provided at each model timestep for
134 the period 2 hours before until 2 hours after sunrise/sunset for each grid point the occultation
135 traversed.

136 Below 25 km, the gradients at both sunrise and sunset terminators are not large, but above this
137 altitude, and in particular at ~ 45 km near the equator, the density changes by several orders of
138 magnitude across the terminator (See Fig. 4, and 6). At sunrise, photolysis of ozone occurs, as
139 seen by its rapid depletion. There is some transport out of the boundary layer above 30 km during
140 the afternoon. At sunset, photolysis stops and the ozone builds up due to the recombination of O
141 and O₂ in the presence of CO₂. There is also a signature of downward transport during the night
142 before sunrise. At southern high latitudes, during the winter, ozone variations at the terminator
143 are almost negligible (Figure 5 and 6 left).

144 4. Retrieval Method Description

145 4.1. Simulation

146 All retrievals of the spectra have been performed using the ASIMUT-ALVL radiative code de-
147 veloped at IASB-BIRA (Vandaele et al., 2006). Initially developed for Earth observation missions
148 (IASI and ACE-FTS, Vandebussche et al. (2013)), the code was later adapted for planetary atmo-
149 spheres, in particular for Venus (Vandaele et al., 2008) and Mars (Drummond et al., 2011; Robert
150 et al., 2017, 2016; Vandaele et al., 2018). ASIMUT-ALVL is a modular program for radiative trans-
151 fer calculations in planetary atmospheres. This code was developed with the objective to be as
152 general as possible, accepting different instrument types (Fourier Transform Spectrometers, grating
153 spectrometers, AOTF combined with an echelle grating) and different viewing geometries (nadir,
154 ground-based, solar occultation/limb). Different radiation contributions are taken into account:
155 direct Sun or reflected on the surface, surface emission and thermal atmospheric emission. Spectra
156 can be simulated/retrieved in the IR, the visible, and in the UV as well. The surface is consid-
157 ered by default to be Lambertian, but a more complex treatment is possible. The determination
158 of the radiation path through the atmosphere, i.e. the path followed by the radiation reaching
159 the instrument, requires that the planet's curvature and refraction are taken into account. The

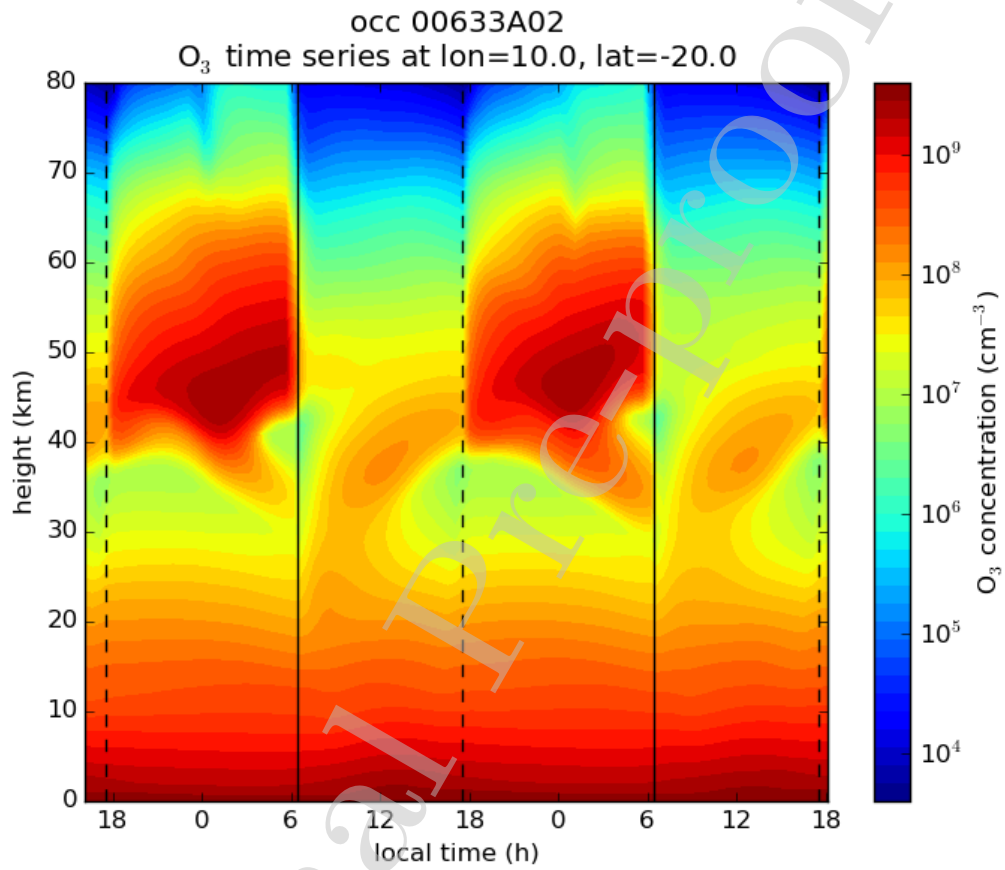


Figure 4: Time series profile of ozone concentration for one GCM model point at the time and location of the SPICAM occultation #00633A02 (solar longitude: 62.3°). The solid (dotted) vertical line represents the sunrise (sunset) terminator.

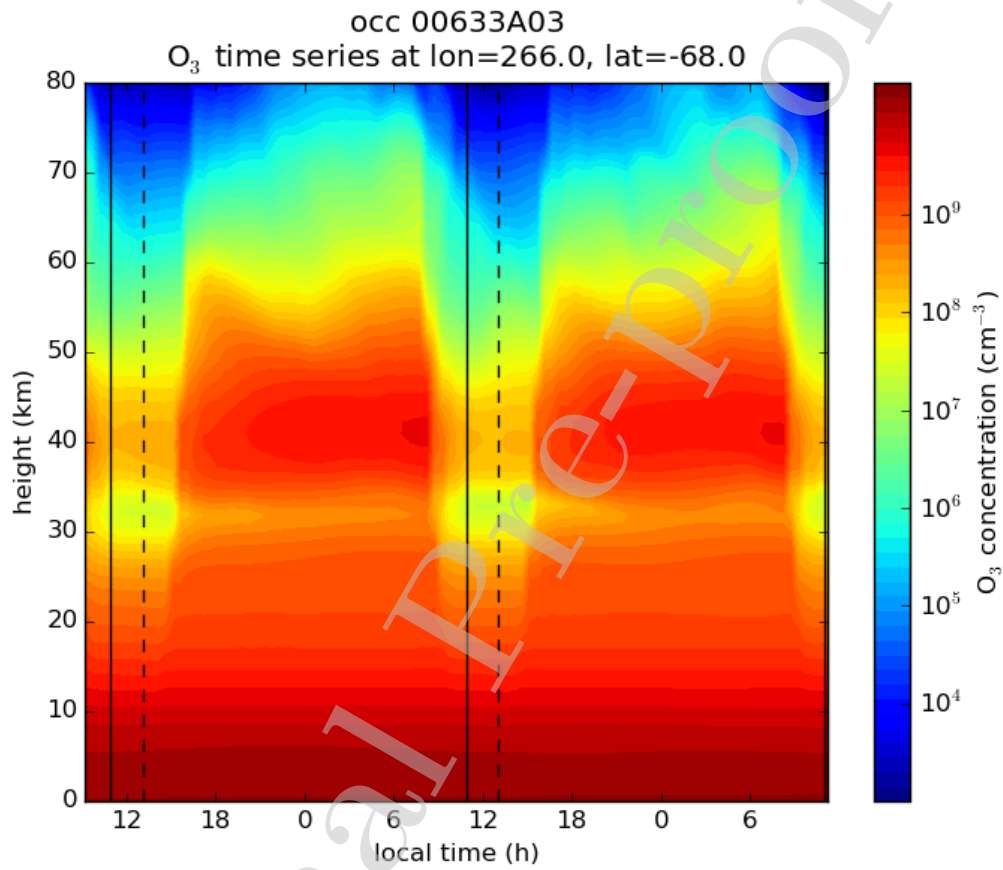


Figure 5: Time series profile of ozone concentration for one GCM model point at the time and location of the SPICAM occultation #00633A03 (solar longitude: 62.3°). The solid (dotted) vertical line represents the sunrise (sunset) terminator.

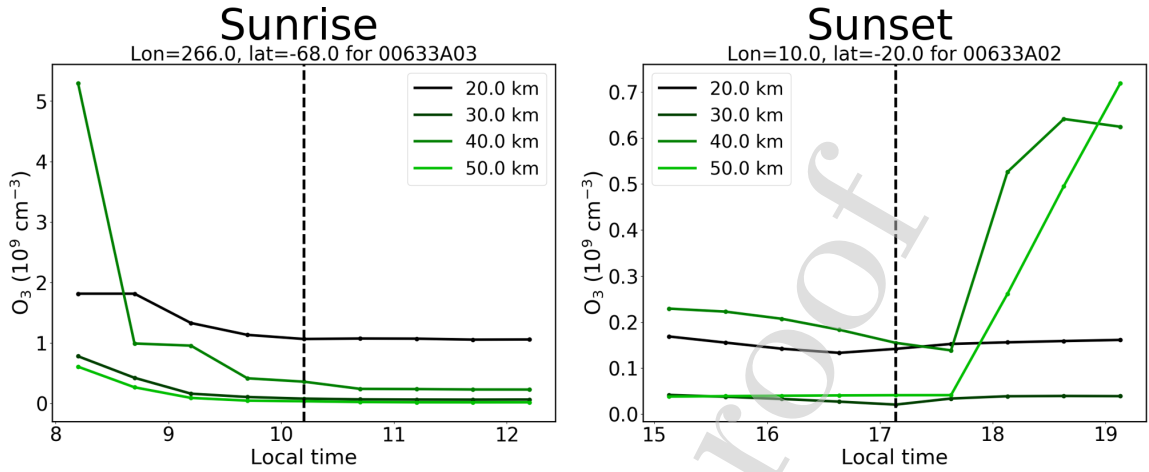


Figure 6: The diurnal variation in the model ozone at sunrise (occultation 00633A03) and at sunset (occultation 00633A02) for different altitudes. The dashed line shows the local time of the terminator.

160 model is based on the ray-tracing program FSCATM (Gallery et al., 1983). ASIMUT-ALVL has
 161 been coupled to SPHER/TMATRIX (Mishchenko and Travis, 1998) and LIDORT (Spurr, 2006)
 162 codes (Kochanova et al., 2011) to include the complete treatment of the scattering effects into the
 163 radiative transfer calculations. Aerosols are included in the ASIMUT-ALVL code, either through
 164 extinction only (ASIMUT) or considering their scattering properties (ALVL, through the call to
 165 LIDORT). The main retrieval module is based on the Optimal Estimation Method (Rodgers, 2000)
 166 coupled to the analytical calculation of the Jacobians. It enables simultaneous or sequential fitting
 167 of different parts of one or more spectra, in order to retrieve the surface temperature, columns or
 168 vertical profiles for molecular species or for aerosols and to fully characterize the outputs (averaging
 169 kernels, errors, DOFS, etc.). The model assumes a one-dimensional atmosphere, with all param-
 170 eters varying only with the vertical variable, the altitude. More detailed information regarding the
 171 retrieval process and the uncertainties calculation can be found in Appendix A.

172 In this work, ASIMUT has been used without calling LIDORT since scattering by the atmo-
 173 sphere was considered negligible in solar occultation. All spectra of one occultation observation
 174 are analysed simultaneously (all transmittances at the various tangent heights) by ASIMUT, which
 175 derives one single O₃ profile to best fit the ensemble of spectra. The atmosphere was structured
 176 in layers whose boundaries were the different tangent altitudes of the observation, adding layers of
 177 1.5 km width above the highest tangent height up to 125.0 km, which was considered the upper

178 limit. Aerosols were not taken into account into the retrieval procedure. ASIMUT enables the user
 179 to fit the baseline spectrum. By configuring this additional fit, impact due to the uncertainties
 180 concerning aerosols could be reduced.

181 The equation describing the radiative transfer through the atmosphere (when no scattering is
 182 present) can be written as:

$$I(\nu) = I_0(\nu)e^{-\tau(\nu,0,z)} + \int_0^z B(\nu, T(s))\alpha(\nu, s)e^{-\tau(\nu,0,z)} ds \quad (2)$$

183 where I_0 represents the light intensity at the starting point of the ray path situated at the
 184 distance z from the observer, $\alpha(\nu, s)$ is the absorption coefficient, $B(\nu, T)$ is the Planck function,
 185 and

$$\tau(\nu, s_1, s_2) = \int_{s_1}^{s_2} \alpha(\nu, s) ds \quad (3)$$

186 is the optical depth along the path between the points s_1 and s_2 . The integration in Eq. 2
 187 occurs along the LOS. The ray tracing (i.e. the determination of the atmosphere characteristics
 188 along the LOS) is done by integrating the temperature, the pressure, the total density, and the
 189 partial densities of all atmospheric constituents in the Curtis-Godson approximation (Goody, 1952;
 190 Godson, 1953). Under this approximation the effective pressure (P^*), the temperature (T^*), and
 191 the density of species k (N_k^*) needed to calculate the optical depth in a layer can be obtained by:

$$P^* = \frac{\int P \cdot \rho \cdot ds}{\int \rho \cdot ds} \quad (4)$$

$$T^* = \frac{\int T \cdot \rho \cdot ds}{\int \rho \cdot ds} \quad (5)$$

$$N_k^* = \frac{\int N_k \cdot \rho \cdot ds}{\int \rho \cdot ds} \quad (6)$$

192 where ρ is the total air density, P , T , and N_k are respectively the pressure, the temperature,
 193 and the density of species k within the layer, and ds is the elementary path length through the
 194 layer on which the integration is done. The calculation of the integral is performed on a sub-grid
 195 of layers separated by 200 m.

196 The optical depth in each of the layers are calculated considering absorption/extinction by O_3 ,
 197 CO_2 and Rayleigh scattering. For CO_2 , the cross-sections from Huestis and Berkowitz (2010) have

198 been selected since they cover a wide spectral interval at relatively high resolution. They are in very
 199 good agreement with the data of Parkinson et al. (2003) obtained at 295 K. O₃ cross-sections have
 200 been built around the temperature dependent data sets of Serdyuchenko et al. (2014), extending the
 201 cross sections towards the shorter wavelength by using either the Reims data set (Brion et al., 1993;
 202 Daumont et al., 1992; Malicet et al., 1995) or the JPL compilation (Sander et al., 2011) depending
 203 on the available temperatures. From these data, a temperature dependent cross-section was built
 204 for O₃ which was used to calculate the optical depth at the temperature of the layer. Rayleigh
 205 scattering was included only as an extinction (no true scattering effects considered) using the data
 206 from Snee and Ubachs (2005). Transmittances corresponding to each sounded altitude were fitted
 207 by considering the absorption of all layers traversed by the LOS of the instrument. They were then
 208 convolved to correspond to the resolution of the SPICAM instrument (0.51 nm).

209 4.2. Gradients as variation along the LOS

210 The treatment of solar occultation observation has been improved in this work by considering
 211 gradients and variations of the density and temperature along the LOS and in particular at the
 212 terminator. Three different gradients can be considered: (1) Temperature gradients across the ter-
 213 minator; (2) (Total) density gradients across the terminator; and (3) Density variations along the
 214 LOS. These gradients will have an impact on the ray tracing procedure (more accurate determina-
 215 tion of the temperature, pressure, and densities within the layers of the atmosphere) and on the
 216 optical depth of the species, since they depend on the temperature and the partial densities of the
 217 species.

218 The correction for the gradients consists of introducing a correction which depends on the top
 219 and bottom altitudes of the layer, which in fact correspond to slightly different Local Solar Times
 220 (LST_{bottom} and LST_{top} , see Figure 7). Two calculations need to be done for the Day and Night
 221 sides respectively. Indeed, at the dawn terminator, the local solar time increases towards the day
 222 side and decreases towards the night side. At dusk, this behaviour reverses..

$$LST_{b/t}^N = LST_{terminator} - f(A_{b/t}^z) \quad (7)$$

$$LST_{b/t}^D = LST_{terminator} + f(A_{b/t}^z) \quad (8)$$

223 where b and t stand for bottom and top respectively, A^z is the angle between the LOS and the

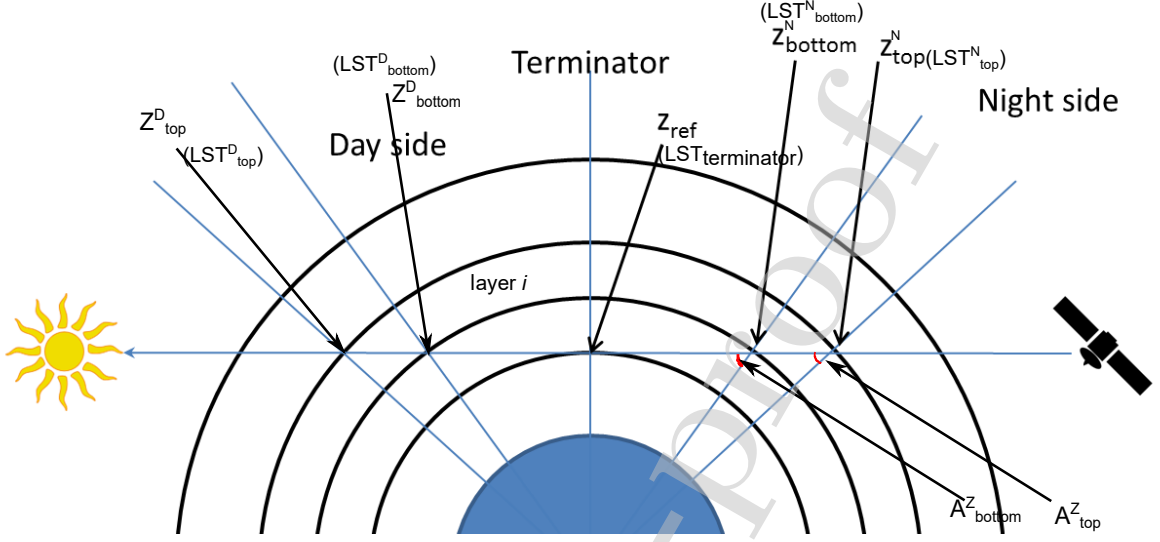


Figure 7: Geometry of a solar occultation; definition of the 'Day' and 'Night' sides.

224 line joining the point along the LOS at altitude z and the center of the planet and f is a function
 225 describing the link between A^z and time defined by the geometry of the observation.

226 In the following, we will introduce 'Day' and 'Night' densities or temperatures (T_i^{*D} , T_i^{*N} ,
 227 $N_{k,i}^{*D}$, $N_{k,i}^{*N}$, for species k and layer i); these will in fact refer respectively to 'after' and 'before' the
 228 terminator (see Figure 7).

229 The different gradients are implemented in the following way. When the user asks to take the
 230 temperature gradient into account, two optical depths are calculated for each layer, corresponding
 231 to the two 'Day' and 'Night' temperatures. These temperatures are calculated using Curtis-Godson
 232 approximation (Eq. 5), where the temperature in the layer is interpolated from the GEM-Mars
 233 simulation data at the LST corrected using Eq. 7-8. Note that the calculation of the 'Night' optical
 234 depth is done only if the two temperatures differ by at least a minimum value which can be specified
 235 by the user (default value set to 2.0 K, minimal value= 0.1 K). Then, the total optical depth (OD)
 236 for the layer i and the species k is the average of the 'Day' and 'Night' side contributions:

$$OD_i^k = \frac{[OD_i^k(T_i^{*D}) \times N_{k,i}^{*D} + OD_i^k(T_i^{*N}) \times N_{k,i}^{*N}]}{2} \quad (9)$$

237 When the user asks to take into account gradients or variations of densities (total density or
238 density of a specific species, such as O_3), the densities of the 'Day' and 'Night' side of the terminator
239 are deduced using the Curtis-Godson approximation (Eq. 6), based on interpolated values of the
240 densities from GEM-Mars simulation data at the LST corrected using Eq. 7-8

241 4.3. Fit strategy

242 Several input parameters are needed to constrain the retrieval: *a priori* vertical profiles of
243 the different species included (CO_2 and O_3) as well as of the temperature and pressure of the
244 atmosphere. All *a priori* information is taken from the GEM-Mars simulations.

245 We assumed as an *a priori* nominal ozone profile the global average ozone VMR from GEM-
246 Mars; i.e. average of all profiles at all Lat/Lon and seasons for one year (MY27). The mean and
247 standard deviation of the ozone volume mixing ratio (VMR), in addition to mean temperature,
248 pressure, and altitude, were derived from the GEM-Mars output of 48 time-steps per day and one
249 day per 10 Ls, for a total of 1728 individual time-steps. The MOLA topographical surface height
250 (Smith et al., 1999) was added to each vertical profile, so that the altitude coordinates are relative
251 to the MGM1025 Mars areoid (Lemoine et al., 2001), and then each individual vertical profile was
252 averaged into 1 km bins from -8 km to 165 km. The vertical profiles were weighted by spherical
253 surface area of the latitude/longitude grid to not oversample the poles due to the regular grid, as
254 well as weighted by the vertical extent of each altitude point to not oversample the near surface
255 profiles due to the adaptive vertical grid. A more detailed description of this derivation, as well as
256 the effects of different methods of averaging and weighting on the *a priori* profiles, will be discussed
257 in a separate article in preparation (Erwin et al., 2018).

258 In a typical retrieval of an (solar) occultation observation, the altitudes at which the O_3 densities
259 are retrieved are the different tangent heights of the different transmittances.

260 5. Ozone retrievals assuming a spherically symmetrical atmosphere

261 As a first step, we performed the retrieval of ozone assuming a spherically symmetrical atmo-
262 sphere. Figure 1 displays transmission spectra at different altitudes (see colorbar) compared to
263 simulated spectra (black solid line) for occultation #00633A02. In addition to the retrieved ozone
264 profiles, ASIMUT produces several metrics that can be used to assess the retrievals. The aver-
265 aging kernels are one of them. Averaging kernels allow to study how the information content is

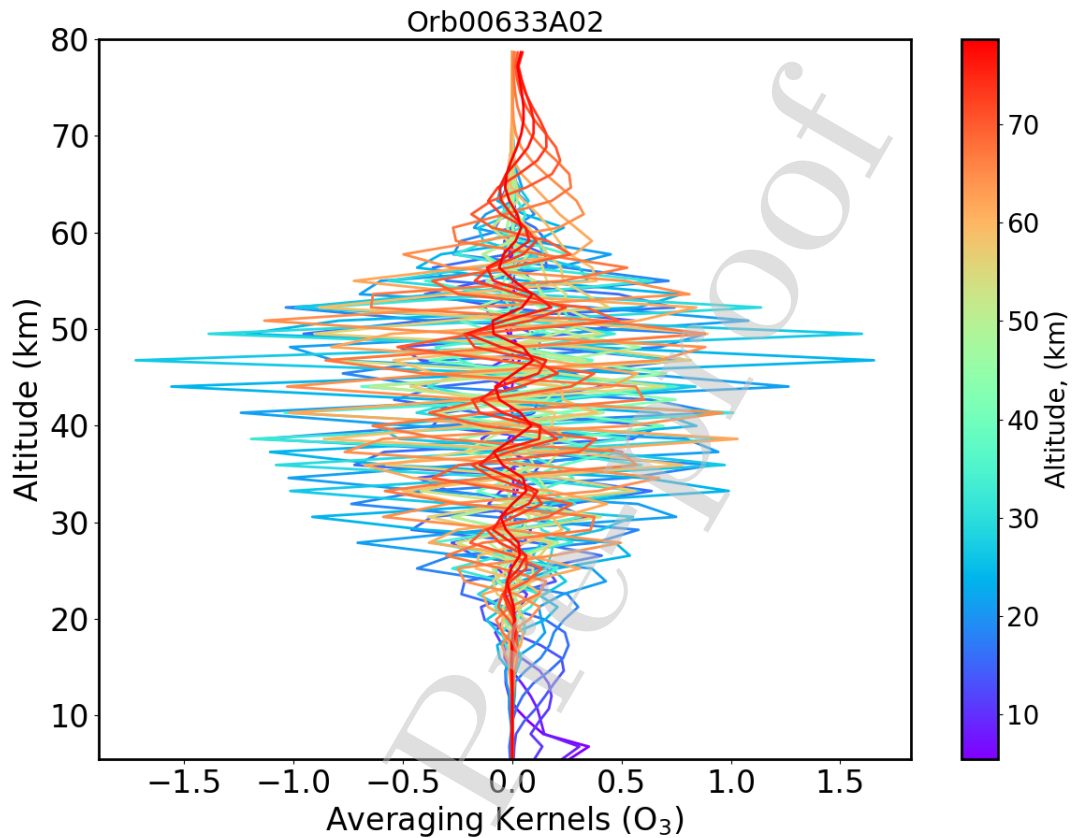


Figure 8: Averaging kernels for occultation #00633A02.

266 distributed in the retrieved profiles. They provide an estimation of the vertical sensitivity of the
 267 retrieval and peak at the altitude of maximum sensitivity. Figure 8 shows the averaging kernel for
 268 occultation #00633A02. From this plot it is evident that the information content is constrained to
 269 the altitude range $\sim 20 - 60$ km. Below this altitude, the horizontal opacity of the dust limits the
 270 measurements.

271 We assessed the sensitivity of the ASIMUT ozone profile retrieval algorithm to a number of
 272 *a priori* assumptions. We studied the impact of the *a priori* ozone profiles, and of the initial
 273 temperature profile on the retrieved ozone profile, as described in more details below.

274 5.1. Sensitivity to the ozone *a priori* profile

275 We tested the dependency of ozone retrievals to the choice of the ozone *a priori* profile. We used
 276 three profiles as *a priori* obtained by multiplying the nominal *a priori* ozone profile by different
 277 factors. In Figure 9 (top) we present two tests respectively for occultation #00633A02 at sunset
 278 and occultation #00633A03 at sunrise. Bottom panels in Figure 9 are similar, but this time we
 279 used as *a priori* profiles constant VMR profiles. In all cases, the retrieved profiles converge within
 280 the expected uncertainty, except at low altitudes during sunrise.

281 5.2. Sensitivity to the temperature profile

282 We tested the sensitivity of the retrieved ozone profiles to the initial choice of temperature profile.
 283 We used as nominal temperature profile the global/temporal average temperature from GEM-Mars.
 284 We then tested two other temperature profiles obtained by adding ± 15 K to the nominal profile.
 285 This value lies within the uncertainty on temperature in GEM-Mars (Neary and Daerden, 2018).
 286 We found a percentage change in the ozone profiles obtained using the two temperature profiles
 287 (blue and red lines in Figure 10) smaller than 25% at 42 km.

288 5.3. Error analysis

289 Errors on the retrieved ozone result from random noise in the measurements and they are
 290 quantified in the inversion method. These random errors are $< 5\%$ between 30 and 40 km; $< 10\%$
 291 below and above these altitudes and they reach a maximum value of 40% at the upper and lower
 292 boundaries. Another source of error on the retrieval of ozone profiles comes from the choice of *a*
 293 *priori* O_3 vmr profile. The retrieved ozone is particularly stable against a change in the *a priori*
 294 O_3 vmr profile (Figure 9). However, uncertainties are mainly dominated by errors due to the initial
 295 temperature profile. A change in the input temperature profile produces a maximum difference of
 296 $\pm 25\%$ on ozone at 42 km (Figure 10).

297 6. Ozone retrievals assuming concentration and temperature gradients around the 298 terminator

299 6.1. Sensitivity to temperature gradients

300 We tested the sensitivity of retrievals to temperature and total density gradients provided by
 301 the GEM-Mars, described in section 3. As mentioned in Section 4.2, if the difference in dayside

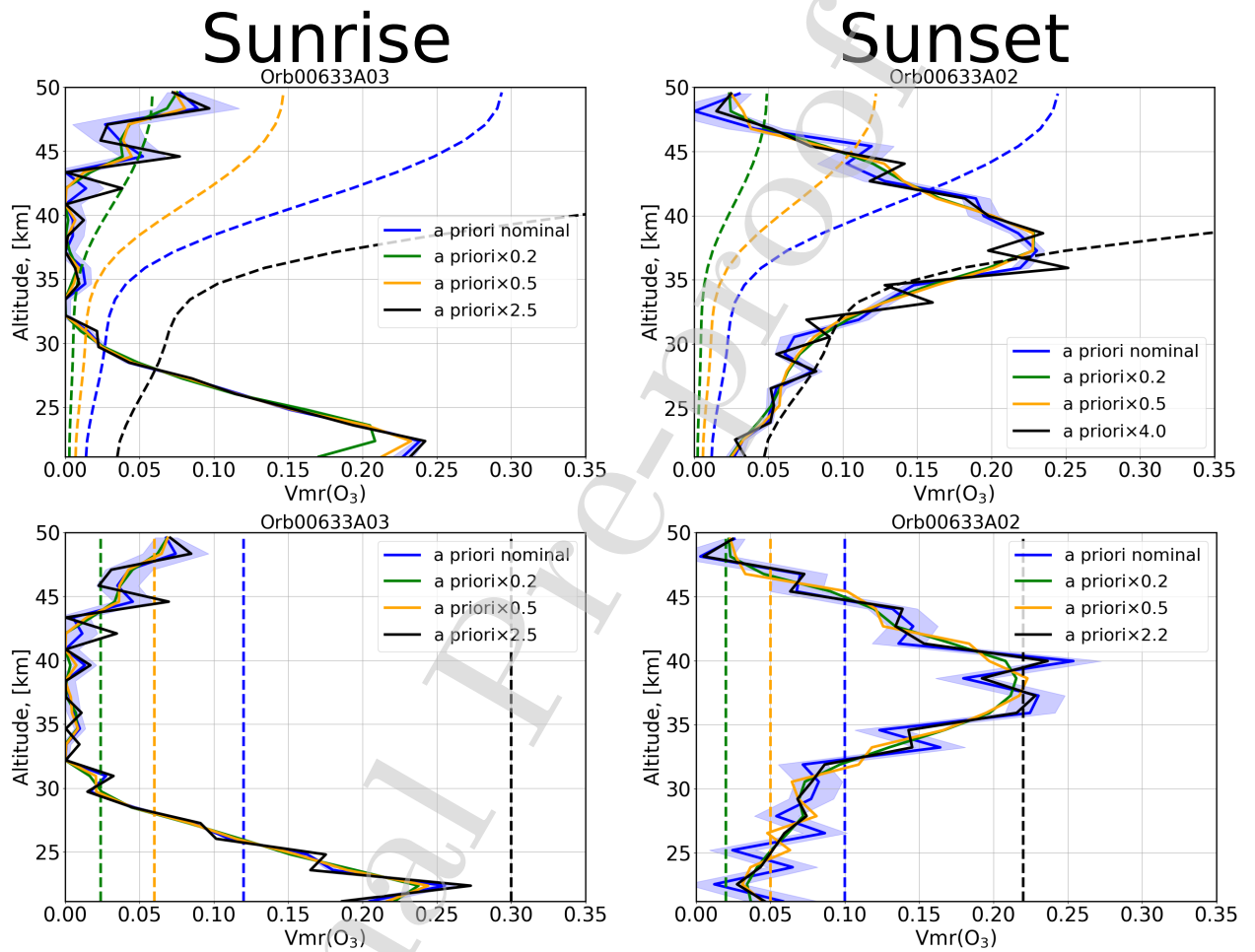


Figure 9: Retrieved ozone profiles [ppm] (solid lines), starting from different first-guess profiles (dashed lines), for occultation #00633A03 (left panels) at sunrise and occultation #00633A02 (right panels) at sunset. Top panels use *a priori* profiles derived from the nominal *a priori* profile (dashed lines). Bottom panels use constant profiles as *a priori*.

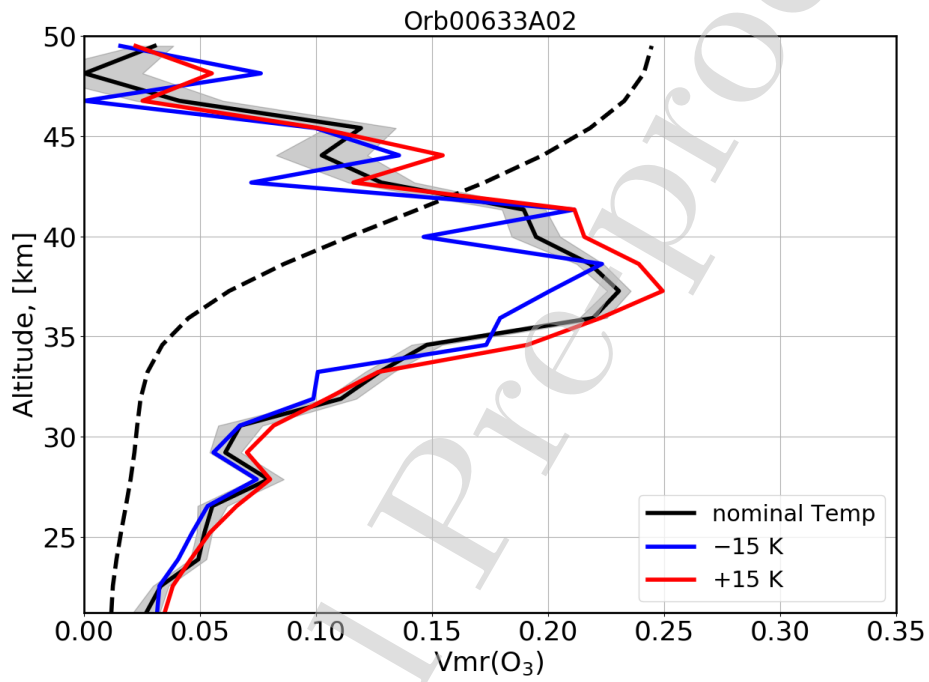


Figure 10: Retrieved ozone profiles [ppm] obtained assuming different first-guess temperatures profiles: (black) nominal temperature; (blue) nominal-15 K; and (red) nominal+15 K. The gray area marks the uncertainty of the retrieved profile. For clarity, only the uncertainty for the nominal profile is shown, similar values are found for the other retrievals. The *a priori* profile (dashed line) is also shown.

302 and nightside temperatures exceeds a threshold, different densities are used for the day and night
303 sides. This threshold is configurable. The default value is set to 2.0 K, we tested in addition a
304 minimal value of 0.1 K. Moreover, we multiplied the GEM-Mars gradients by a factor of 2 and
305 5. Temperature gradients do not have any impact on the retrievals of ozone (figures are not
306 shown here). This can be explained by the small temperature dependence of the O_3 cross sections.
307 Nevertheless, we included temperature gradients in the retrieval process.

308 *6.2. Sensitivity to O_3 gradients*

309 We investigated the impact of taking into account the variations of ozone concentrations along
310 the LOS at the day/night terminator. As input, we provided the ozone gradients calculated by the
311 GEM-Mars (see section 3). The differences in the model between the ozone variations for sunset and
312 sunrise conditions, as well as for different locations (see Figures 4 and 5), suggest that the effects
313 of gradients on the retrievals should change for different occultations. The steeper gradient for the
314 selected sunset occultations at low latitudes indicates the impact of gradients will be stronger for
315 these occultations compared to sunrise data (Fig. 6).

316 Figures 11 and 12 show retrieved ozone profiles for different occultations respectively at sunset
317 and sunrise. Ozone profiles (solid red line) derived using GEM-Mars gradients are compared to
318 profiles obtained assuming a spherically symmetrical atmosphere (blue dashed line). The insert
319 panels show the vmr differences in percent between the two retrievals. At sunset (Figure 11),
320 retrievals show an ozone layer located in the altitude range 35 – 50 km. The inclusion of gradients
321 in the retrieval method results in a $< 20\%$ reduction in ozone mixing ratio for sunset condition.
322 Except for occultation #00584A02, the impact of retrievals lies within the error bar. The rapid
323 variations observed for occultation #00655A01 are due to the retrieval procedure.

324 At sunrise (Figure 12), profiles show the presence of an ozone layer located near the surface, the
325 top of which is located at altitudes below 30 km. The impact of gradients on retrievals at sunrise
326 is negligible. This behavior can be explained by the specific locations of sunrise occultations. In
327 fact, as shown in Figure 5, the day length is much shorter compared to the night at these latitudes
328 and season and the ozone gradient is not very sharp.

329 In order to test the sensitivity of the retrievals on the initial ozone gradient, we multiplied the
330 difference between day and night ozone along the LOS (provided by GEM-Mars) by factors of 2
331 and 3. Factors 1, 2, and 3 produce a percentage change with respect to the nominal profile of

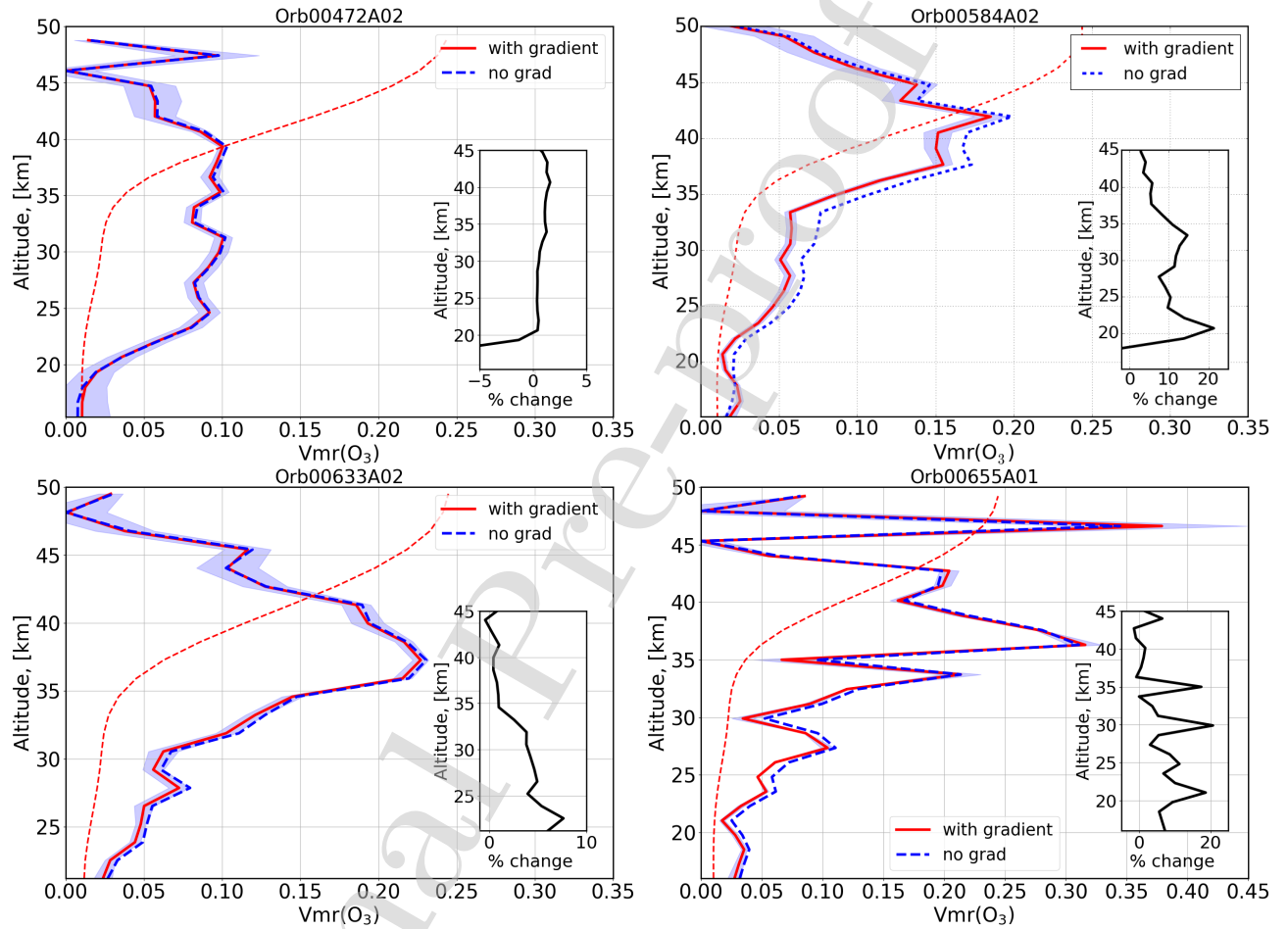


Figure 11: Retrieved ozone profiles [ppm] for different occultations at sunset derived using GEM-Mars gradients (red solid lines) compared to profiles retrieved assuming a spherically symmetrical atmosphere (blue dashed lines). The *a priori* profile used for the retrieval is also shown (red dashed line). The insert panel shows the vmr difference in percent between the two retrievals.

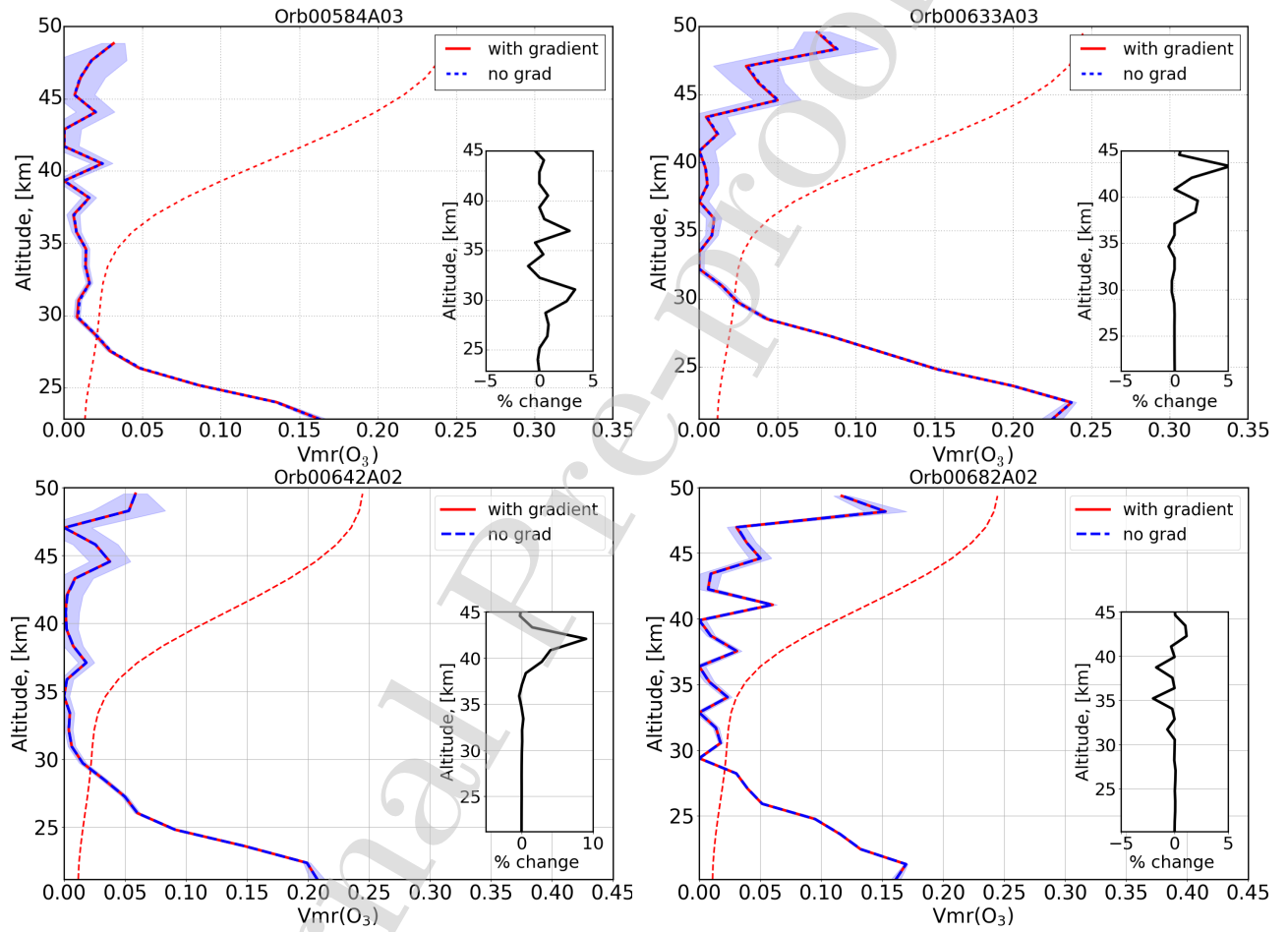


Figure 12: As in Fig. 11 but for occultations acquired at sunrise.

332 respectively: $< 7\%$, $< 30\%$, and $< 59\%$ at altitudes below 30 km (See Fig. 13).

333 The effect of gradients on the retrievals depends on the inputs gradients provided by the pho-
334 tochemical model, in our case GEM-Mars. The model gradients, moreover, strongly depend on the
335 latitude, altitude, and season of the occultations, since ozone is dependent on all these factors.

336 7. Comparison to a different retrieval strategy

337 In order to validate different retrieval methods, we compared our results with the profiles of
338 ozone from SPICAM solar occultations analysed by Määttä et al. (submitted to Icarus, 2019)
339 (LATMOS retrievals from now on). It is important to notice that the spectral fitting strategy for
340 LATMOS retrievals is different from the one applied in this study: LATMOS retrievals result in
341 profiles of concentrations of ozone integrated along the LOS (slant profiles). ASIMUT provides
342 both vertical and slant profiles. To compare the results obtained from the two methods, in this
343 section we are therefore showing ASIMUT slant retrievals.

344 The data analysis method for the LATMOS retrievals are discussed in Quémerais et al. (2006);
345 Montmessin et al. (2006); Määttä et al. (2013, submitted to Icarus, 2019) and are only briefly
346 summarized here. The transmission spectra are calculated by averaging the solar spectrum mea-
347 sured above 120 km, and then dividing all the spectra by this reference spectrum. Only spectra
348 void of spurious high-gain peaks or oscillations caused by the MARSIS radar antennae are used in
349 the procedure (see Määttä et al. (2013)). To obtain the LOS ozone columns, the transmission
350 spectra are fitted with a model based on the Beer-Lambert (BL) law that in this case describes
351 the total absorption on the LOS by gases (CO_2 , O_3) and by aerosols (using the so-called α -model:
352 O'Neill and Royer (1993); Dubovik et al. (2000)). The BL model does not include any assumptions
353 of gradients along the line of sight, since it simply describes the transmissions as the result of the
354 sum of the extinctions caused by the total concentrations of species on the LOS. The BL model is
355 fitted to the transmissions by using a Levenberg-Marquardt method (IDL routine MPFIT, Mar-
356 wardt (2009)) and adjusting simultaneously the four unknowns: total concentrations of CO_2 and
357 O_3 , the dust optical depth and the α coefficient. As the fitting is started from the top of the atmo-
358 sphere (transmission is essentially equal to one, so no absorption is expected) the *a priori* values
359 for O_3 and dust are started from a very small value (practically zero) at the top of the atmosphere.
360 Once the fitting procedure finds positive values for these variables, the fitting for each subsequent
361 layer starts with the value of the previous layer as a first guess. Since the Sun is quite dim in the

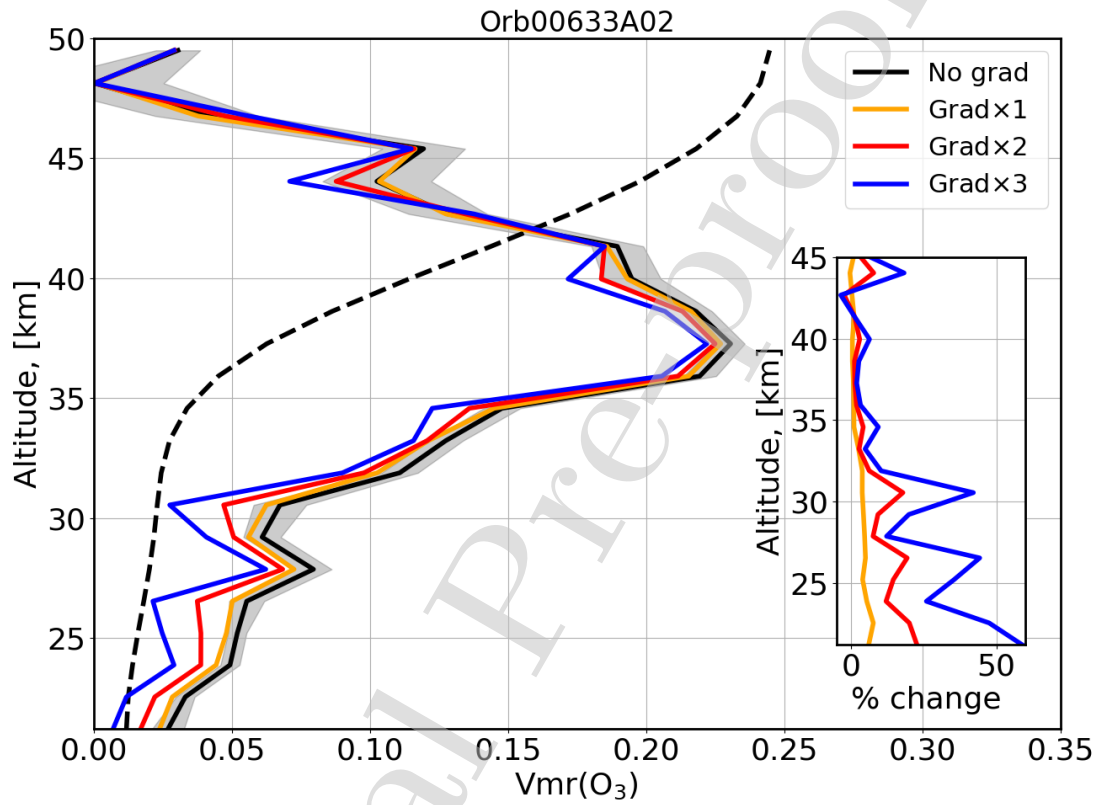


Figure 13: Retrieved ozone profiles [ppm] for occultation #0633A02 derived using GEM-Mars gradients compared to the profile retrieved assuming a spherically symmetrical atmosphere (black line). GEM-Mars gradients were multiplied by different factors: 1 (yellow line), 2 (red line), and 3 (blue line). The *a priori* profile used for the retrieval is also shown (black dashed line). The insert panel shows the VMR difference in percent between the retrievals.

362 UV, the transmission spectra are very noisy within the CO₂ absorption band below 200 nm, often
363 preventing the fitting routine from converging. We improved the CO₂ fits significantly by defining
364 the *a priori* for CO₂ from profiles of the Mars Climate Database (MCD v4.3, Millour et al. (2008);
365 see details in Määttä et al. (2013)). The fitting provides LOS column concentrations of CO₂
366 and O₃, and LOS aerosol optical depth and a value for α , and the corresponding uncertainties (see
367 Määttä et al. (2013) for details on the error estimation).

368 Figure 14 displays the comparison between ozone slant densities for three occultations at sun-
369 rise and sunset. Different colors correspond respectively to: (black) ASIMUT retrievals assuming a
370 spherically symmetrical atmosphere; (red) ASIMUT retrievals including GEM-Mars gradients; and
371 (orange) LATMOS retrievals assuming a spherically symmetrical atmosphere. The perfect agree-
372 ment between ASIMUT retrievals assuming a spherically symmetrical atmosphere and ASIMUT
373 retrievals including GEM-Mars gradients was expected, since gradients should not impact the LOS
374 optical thickness. ASIMUT and LATMOS retrievals are in very good agreement. Differences,
375 especially for sunset occultations, may be explained by different *a priori* inputs.

376 8. Summary

377 Rapid changes in the species concentration at the day-night terminator driven by differences in
378 the solar illumination may cause asymmetries along the LOS of a solar occultation experiment that
379 need to be taken into account in the retrieval process. In the present manuscript, we applied an
380 improved retrieval scheme that handles concentration gradients along the LOS to the retrieval of
381 ozone from SPICAM/MEx solar occultations. We used the GEM-Mars three-dimensional General
382 Circulation Model to quantify the input gradients across the terminator for our retrievals. Our
383 model results strongly depend on the latitude, altitude, and season of the occultations, since ozone
384 is affected by all these factors. Ozone does not show strong variations with solar zenith angle (local
385 solar time) at altitudes below 25 km. Above this altitude, especially around ~ 45 km near the
386 equator, the density changes by several orders of magnitude across the terminator. In addition,
387 near the equator, differences between sunrise and sunset variation in ozone concentration are evident
388 and they can be explained by the ozone photochemistry. In the high latitude southern hemisphere,
389 during the winter, ozone variations at the terminator are almost negligible.

390 The impact of gradients on the retrievals strongly follows the GCM model results. Uncertainties
391 in the model ozone diurnal variations may affect the corrections to the retrieved profile. All selected

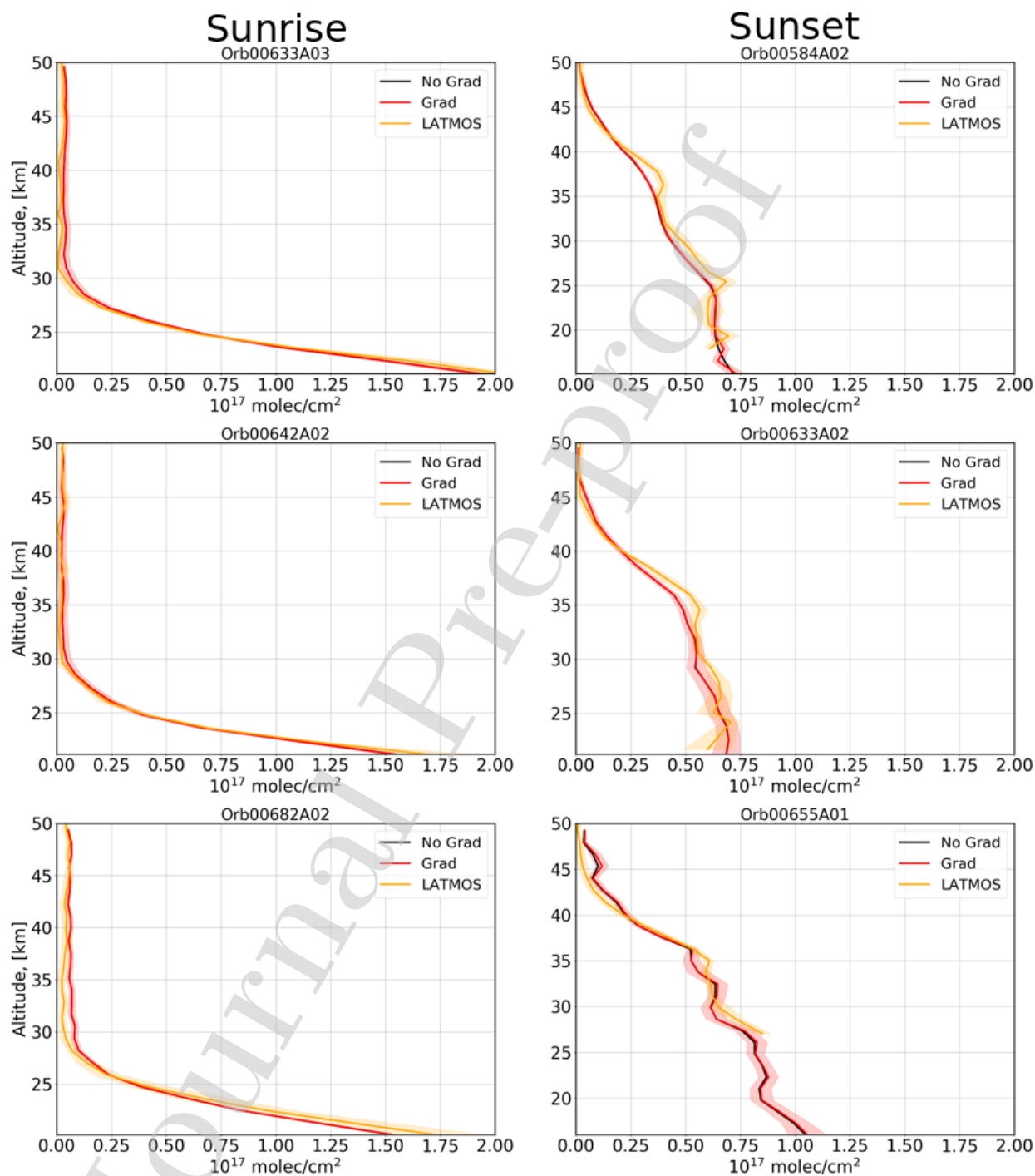


Figure 14: Examples of retrieved ozone slant densities derived using GEM-Mars gradients (red lines) compared to profiles derived at LATMOS (orange lines). ASIMUT profile retrieved assuming a spherically symmetrical atmosphere (blue lines) are also shown.

392 sunset occultations are located near the equator while sunrise occultations are situated at high
393 latitudes south. The sunset ozone retrieved vmr reach up to 20% difference when the asymmetry
394 of the atmosphere is considered. At sunrise, the impact of gradients on the retrievals is negligible.
395 This behavior can be explained by the specific location of sunrise occultations, all situated at high
396 latitudes in the South. It is expected from the GCM model that gradients are important for sunrise
397 retrievals near the equator.

398 In order to study the effects of ozone gradients at different latitudes and seasons, and in particular
399 to investigate the differences between sunrise/sunset conditions, we plan to extend the analysis to
400 the whole SPICAM database and to NOMAD/ExoMars observations.

401 **Acknowledgments**

402 The research leading to these results has received funding from the European Unions Horizon
403 2020 Programme (H2020-Compet-08-2014) under grant agreement UPWARDS-633127. SA is sup-
404 ported by the FNRS CRAMIC project under grant number T.0171.16. This project acknowledges
405 funding by the Belgian Science Policy Office (BELSPO), with financial and contractual coordina-
406 tion by the ESA Prodex Office (PEA4000121493). This work was supported by the Belgian Fonds
407 de la Recherche Scientifique FNRS under grant number 30442502 (ET_HOME) and through the
408 BRAIN Research contract BR/143/A2/SCOOP.

409 SPICAM-UV dataset is available through the European Space Agency's Planetary Science
410 Archive (PSA). Ozone profiles will be later available through the VESPA (Virtual European Solar
411 and Planetary Access) interface (<http://vespa.obspm.fr>).

412 **Appendix A. Retrieval**

413 The ASIMUT retrieval module is based on the use of the Optimal Estimation Method , in
 414 which *a priori* information is used to represent the best statistical knowledge of the state of the
 415 atmosphere to be retrieved, prior to any measurement. The purpose of the retrieval is then to find
 416 the approximation of the true state at the atmosphere which agrees best with both the measurement
 417 and the *a priori* information. The general forward radiative transfer equation can be written as:

$$\mathbf{y} = \mathbf{f}(\mathbf{x}, \mathbf{b}) + \epsilon \quad (\text{A.1})$$

418 where \mathbf{y} is the measurement vector (the measured radiance), \mathbf{x} is the state vector (the vertical
 419 profiles to be retrieved), \mathbf{b} represents the additional parameters used by the forward model \mathbf{f} , and
 420 ϵ is the random measurement noise. The forward function \mathbf{f} describes the complete physics of the
 421 measurement, including the description of the instrument. \mathbf{b} is a vector of model parameters (such
 422 as spectral line data, calibration parameters, etc.) that are not perfectly known by the observer.
 423 They are a possible source of random or systematic differences between calculated and measured
 424 values of \mathbf{y} .

425 In the case of a moderately nonlinear problem, the best estimate $\hat{\mathbf{x}}$ of the solution of Eq. A.1 is
 426 found by solving iteratively

$$\mathbf{x}_{i+1} = \mathbf{x}_a + \mathbf{G}_i[\mathbf{y} - \mathbf{f}(\mathbf{x}_i) + \mathbf{K}_i(\mathbf{x}_i - \mathbf{x}_a)] \quad (\text{A.2})$$

427 where \mathbf{x}_a is the *a priori* constraint. The Jacobian matrix \mathbf{K} is defined by the following expression:

$$\mathbf{K} = \frac{\partial \mathbf{f}}{\partial \mathbf{x}} \quad (\text{A.3})$$

428 and the Gain matrix \mathbf{G} is defined by:

$$\mathbf{G}_i = (\mathbf{S}_a^{-1} + \mathbf{K}_i^T \mathbf{S}_e^{-1} \mathbf{K}_i)^{-1} \mathbf{K}_i^T \mathbf{S}_e^{-1} \quad (\text{A.4})$$

429 where \mathbf{S}_e is the error covariance matrix of the measurements, and \mathbf{S}_a the *a priori* covariance
 430 matrix. \mathbf{S}_e is usually chosen to be diagonal, characterizing all the sources of systematic and random
 431 errors on the measured radiance.

432 The *a priori* covariance matrices (\mathbf{S}_a) represents the variability of the gas/aerosol considered.
 433 Here ASIMUT considered diagonal matrices with off-diagonal terms added as Gaussian

$$S_a(i, j) = \sqrt{S_a(i, i)S_a(j, j)} \exp\left(-\left(\frac{z_i - z_j}{l_c}\right)^2\right) \quad (\text{A.5})$$

434 to account for correlations between the concentrations at different altitudes (z_i is the altitude
 435 of level i , l_c is the vertical correlation length).

436 The convergence is attained when the two following conditions are met:

$$d_i^2 = (\mathbf{x}_i - \mathbf{x}_{i+1})^T \mathbf{S}^{-1} (\mathbf{x}_i - \mathbf{x}_{i+1}) \lll n \quad (\text{A.6a})$$

$$d_i^2 = (\mathbf{f}(\mathbf{x}_{i+1}) - \mathbf{f}(\mathbf{x}_i))^T \mathbf{S}_{\delta y}^{-1} (\mathbf{f}(\mathbf{x}_{i+1}) - \mathbf{f}(\mathbf{x}_i)) \ll m \quad (\text{A.6b})$$

437 with n the number of parameters to retrieve, m the number of observed points, and

$$\delta y = \mathbf{y} - \mathbf{f}(\hat{\mathbf{x}}) \quad (\text{A.7})$$

$$\mathbf{S}_{\delta y} = \mathbf{S}_e (\mathbf{K} \mathbf{S}_a \mathbf{K}^T)^{-1} \mathbf{S}_e \quad (\text{A.8})$$

438 The first expression represents the convergence condition on the fitted parameters, and the
 439 second on the difference between observed and simulated spectra.

440 The total error decomposes into several contributions, i.e. the smoothing error ($\mathbf{S}_{smoothing}$), the
 441 measurement error (\mathbf{S}_{measur}) and the forward model parameters error (\mathbf{S}_{model}).

$$\mathbf{S} = \mathbf{S}_{smoothing} + \mathbf{S}_{measur} + \mathbf{S}_{model} \quad (\text{A.9})$$

442 In this work we have not considered the last term (\mathbf{S}_{model}). The measurement error propagates
 443 from the instrumental noise. Its covariance is given by:

$$\mathbf{S}_{measur} = \mathbf{G} \mathbf{S}_e \mathbf{G}^T \quad (\text{A.10})$$

444 The smoothing error accounts for the sensitivity of the measurements/forward model to the
 445 variable to be retrieved (i.e. the measurement/forward model system does not allow perfectly

446 reproducing the true atmosphere, but a smoothed value of it). The resulting error is characterized
 447 by the following covariance matrix:

$$\mathbf{S}_{smoothing} = (\mathbf{A} - \mathbf{I})\mathbf{S}_a(\mathbf{A} - \mathbf{I})^{-1} \quad (\text{A.11})$$

448 where \mathbf{I} is the identity matrix, and \mathbf{A} is the averaging kernel matrix. It is defined as the
 449 sensitivity of the retrieved state (hereafter symbolized by $\hat{\mathbf{x}}$) to the true state (\mathbf{x}) and can be
 450 calculated as:

$$\mathbf{A} = \frac{\partial \hat{\mathbf{x}}}{\partial \mathbf{x}} = \mathbf{G}\mathbf{K} \quad (\text{A.12})$$

451 The rows of \mathbf{A} define an averaging kernel function (AVK) for each element of $\hat{\mathbf{x}}$, which peaks at
 452 the altitude from where most of the information is coming. In other words, the AVK provide an
 453 estimation of the vertical sensitivity of the retrieval and peak at the altitude of maximum sensitivity.
 454 The trace of the \mathbf{A} matrix gives the degrees of freedom for signal (DOFS), defined as the number
 455 of independent pieces of information in the retrieved profile.

456 Finally the sum of these covariances associated to these different uncertainties provide an esti-
 457 mation of the total error on the retrieved parameters. One can show that the covariance matrix
 458 associated to $\hat{\mathbf{x}}$ is given by:

$$\mathbf{S} = (\mathbf{S}_a^{-1} + \mathbf{K}_i^T \mathbf{S}_e^{-1} \mathbf{K}_i)^{-1} \quad (\text{A.13})$$

459 The square root of the diagonal elements of \mathbf{S} can be seen as the error on the retrieved param-
 460 eters.

461 References

462 Bertaux, J.L., Korablev, O., Perrier, S., Quémerais, E., Montmessin, F., Leblanc, F., Lebonnois,
 463 S., Rannou, P., Lefèvre, F., Forget, F., Fedorova, A., Dimarellis, E., Reberac, A., Fonteyn, D.,
 464 Chaufray, J.Y., Guibert, S., 2006. SPICAM on Mars Express: Observing modes and overview
 465 of UV spectrometer data and scientific results. *Journal of Geophysical Research (Planets)* 111.
 466 doi:10.1029/2006JE002690.

- 467 Boughner, R., Larsen, J.C., Natarajan, M., 1980. The influence of NO and C₂O variations at
468 twilight on the interpretation of solar occultation measurements. *Geophysical Research Letters*
469 7, 231–234. doi:10.1029/GL007i004p00231.
- 470 Brion, J., Chakir, A., Daumont, D., Malicet, J., Parisse, C., 1993. High-resolution laboratory
471 absorption cross section of O₃. Temperature effect. *Chemical Physics Letters* 213, 610–612.
472 doi:10.1016/0009-2614(93)89169-I.
- 473 Daerden, F., Neary, L., Viscardy, S., García Muñoz, A., Clancy, R.T., Smith, M.D., Encrenaz,
474 T., Fedorova, A., 2019. Mars atmospheric chemistry simulations with the GEM-Mars general
475 circulation model. *Icarus* 326, 197–224. doi:10.1016/j.icarus.2019.02.030.
- 476 Daumont, D., Brion, J., Charbonnier, J., Malicet, J., 1992. Ozone UV spectroscopy. I - Absorption
477 cross-sections at room temperature. *Journal of Atmospheric Chemistry* 15, 145–155. doi:10.
478 1007/BF00053756.
- 479 Drummond, R., Vandaele, A.C., Daerden, F., Fussen, D., Mahieux, A., Neary, L., Neefs, E.,
480 Robert, S., Willame, Y., Wilquet, V., 2011. Studying methane and other trace species in the
481 Mars atmosphere using a SOIR instrument. *Planetary and Space Science* 59, 292–298. doi:10.
482 1016/j.pss.2010.05.009.
- 483 Dubovik, O., Smirnov, A., Holben, B.N., King, M.D., Kaufman, Y.J., Eck, T.F., Slutsker, I.,
484 2000. Accuracy assessments of aerosol optical properties retrieved from Aerosol Robotic Network
485 (AERONET) Sun and sky radiance measurements. *Journal of Geophysical Research* 105, 9791–
486 9806. doi:10.1029/2000JD900040.
- 487 Erwin, J., Neary, L., Daerden, F., Viscardy, S., Carine Vandaele, A., 2018. Creating high-spatial
488 resolution atmospheric profiles from the GEM-Mars GCM for the investigation of Mars, in:
489 European Planetary Science Congress, pp. EPSC2018–717.
- 490 Forget, F., Montmessin, F., Bertaux, J.L., González-Galindo, F., Lebonnois, S., Quémerais, E.,
491 Reberac, A., Dimarellis, E., López-Valverde, M.A., 2009. Density and temperatures of the upper
492 Martian atmosphere measured by stellar occultations with Mars Express SPICAM. *Journal of*
493 *Geophysical Research (Planets)* 114, 1004. doi:10.1029/2008JE003086.

- 494 Gallery, W.O., Kneizys, F.X., Clough, S.A., 1983. Air mass computer program for atmospheric
495 transmittance/radiance calculation: FSCATM. Technical Report.
- 496 Godson, W.L., 1953. The evaluation of infra-red radiative fluxes due to atmospheric water
497 vapour. Quarterly Journal of the Royal Meteorological Society 79, 367–379. doi:10.1002/qj.
498 49707934104.
- 499 Goody, R.M., 1952. A statistical model for water-vapour absorption. Quarterly Journal
500 of the Royal Meteorological Society 78, 638–640. URL: <https://rmets.onlinelibrary.wiley.com/doi/abs/10.1002/qj.49707833820>,
501 doi:10.1002/qj.49707833820,
502 arXiv:<https://rmets.onlinelibrary.wiley.com/doi/pdf/10.1002/qj.49707833820>.
- 503 Huestis, D.L., Berkowitz, J., 2010. Critical Evaluation of the Photoabsorption Cross Section of
504 CO₂ from 0.125 to 201.6 nm at Room Temperature, in: AAS/Division for Planetary Sciences
505 Meeting Abstracts #42, p. 48.13.
- 506 Kochenova, S., De Mazière, M., Vandaele, A., Kerzenmacher, T., Letocart, V., Kumps, N., Willame,
507 Y., 2011. Alvl 1.0: an advanced line-by-line radiative transfer model for the retrieval of atmo-
508 spheric constituents from satellite and ground-based measurements.
- 509 Lebonnois, S., Quémerais, E., Montmessin, F., Lefèvre, F., Perrier, S., Bertaux, J.L., Forget,
510 F., 2006. Vertical distribution of ozone on Mars as measured by SPICAM/Mars Ex-
511 press using stellar occultations. Journal of Geophysical Research (Planets) 111, E09S05.
512 doi:10.1029/2005JE002643.
- 513 Lefèvre, F., Lebonnois, S., Montmessin, F., Forget, F., 2004. Three-dimensional modeling of ozone
514 on Mars. Journal of Geophysical Research (Planets) 109, E07004. doi:10.1029/2004JE002268.
- 515 Lemoine, F.G., Neumann, G.A., Chinn, D.S., Smith, D.E., Zuber, M.T., Rowlands, D.D., Rubin-
516 cam, D.P., Pavlis, D.E., 2001. Solutions for Mars Geophysical Parameters from Mars Global
517 Surveyor Tracking Data, in: AGU Fall Meeting Abstracts, p. P42A.
- 518 Määttänen, A., Lefèvre, F., Montmessin, F., Listowski, C., Guilbon, S., Fedorova, A., Korablev,
519 O., submitted to Icarus, 2019. Climatology of the ozone vertical distribution on Mars from
520 SPICAM/MEX UV occultations. Submitted to Icarus, this issue, 2019.

- 521 Määttänen, A., Listowski, C., Montmessin, F., Maltagliati, L., Reberac, A., Joly, L., Bertaux, J.L.,
522 2013. A complete climatology of the aerosol vertical distribution on Mars from MEx/SPICAM
523 UV solar occultations. *Icarus* 223, 892–941. doi:10.1016/j.icarus.2012.12.001.
- 524 Malicet, J., Daumont, D., Charbonnier, J., Parisse, C., Chakir, A., Brion, J., 1995. Ozone UV
525 spectroscopy. II. Absorption cross-sections and temperature dependence. *Journal of Atmospheric*
526 *Chemistry* 21, 263–273. doi:10.1007/BF00696758.
- 527 Markwardt, C.B., 2009. Non-linear Least-squares Fitting in IDL with MPFIT, in: Bohlender, D.A.,
528 Durand, D., Dowler, P. (Eds.), *Astronomical Data Analysis Software and Systems XVIII*, p. 251.
529 arXiv:0902.2850.
- 530 Millour, E., Forget, F., González-Galindo, F., Spiga, A., Lebonnois, S., Montabone, L., Lewis, S.R.,
531 Read, P.L., López-Valverde, M.A., Gilli, G., Lefèvre, F., Montmessin, F., Desjean, M.C., Huot,
532 J.P., McD/Gcm Development Team, 2008. The Latest (Version 4.3) Mars Climate Database, in:
533 *Third International Workshop on The Mars Atmosphere: Modeling and Observations*, p. 9029.
- 534 Mishchenko, M., Travis, L.D., 1998. Capabilities and limitations of a current FORTAN implemen-
535 tation of the T-matrix method for randomly oriented, rotationally symmetric scatterers. *Journal*
536 *of Quantitative Spectroscopy and Radiative Transfer* 60, 309–324. doi:10.1016/S0022-4073(98)
537 00008-9.
- 538 Montmessin, F., Bertaux, J.L., Quémerais, E., Korablev, O., Rannou, P., Forget, F., Perrier, S.,
539 Fussen, D., Lebonnois, S., Rébérac, A., Dimarellis, E., 2006. Subvisible CO₂ ice clouds detected
540 in the mesosphere of Mars. *Icarus* 183, 403–410. doi:10.1016/j.icarus.2006.03.015.
- 541 Natarajan, M., Deaver, L.E., Thompson, E., Magill, B., 2005. Impact of twilight gradients on the
542 retrieval of mesospheric ozone from HALOE. *Journal of Geophysical Research (Atmospheres)*
543 110, D13305. doi:10.1029/2004JD005719.
- 544 Neary, L., Daerden, F., 2018. The GEM-Mars general circulation model for Mars: Description and
545 evaluation. *Icarus* 300, 458–476. doi:10.1016/j.icarus.2017.09.028.
- 546 Nevejans, D., Neefs, E., van Ransbeeck, E., Berkenbosch, S., Clairquin, R., de Vos, L., Moelans,
547 W., Glorieux, S., Baeke, A., Korablev, O., Vinogradov, I., Kalinnikov, Y., Bach, B., Dubois,
548 J.P., Villard, E., 2006. Compact high-resolution spaceborne echelle grating spectrometer with

- 549 acousto-optical tunable filter based order sorting for the infrared domain from 2.2 to 4.3 μm .
550 *Applied Optics* 45, 5191–5206. doi:10.1364/AO.45.005191.
- 551 O’Neill, N., Royer, A., 1993. Extraction of bimodal aerosol-size distribution radii from spectral
552 and angular slope (Angstrom) coefficients. *Applied Optics* 32, 1642–1645. doi:10.1364/AO.32.
553 001642.
- 554 Parkinson, W.H., Rufus, J., Yoshino, K., 2003. Absolute absorption cross section measurements of
555 CO_2 in the wavelength region 163–200 nm and the temperature dependence. *Chemical Physics*
556 290, 251–256. doi:10.1016/S0301-0104(03)00146-0.
- 557 Quémerais, E., Bertaux, J.L., Korabely, O., Dimarellis, E., Cot, C., Sandel, B.R., Fussen, D., 2006.
558 Stellar occultations observed by SPICAM on Mars Express. *Journal of Geophysical Research*
559 (Planets) 111, 9. doi:10.1029/2005JE002604.
- 560 Robert, S., Camy-Peyret, C., Daerden, F., De Mazière, M., De Wachter, E., Neary, L., Vandebuss-
561 che, S., Vandaele, A.C., 2017. Two test-cases for synergistic detections in the Martian atmosphere:
562 Carbon monoxide and methane. *Journal of Quantitative Spectroscopy and Radiative Transfer*
563 189, 86–104. doi:10.1016/j.jqsrt.2016.11.003.
- 564 Robert, S., Vandaele, A.C., Thomas, I., Willame, Y., Daerden, F., Delanoye, S., Depiesse, C.,
565 Drummond, R., Neefs, E., Neary, L., Ristic, B., Mason, J., Lopez-Moreno, J.J., Rodriguez-
566 Gomez, J., Patel, M.R., Bellucci, G., Vandaele, A.C., Lopez Moreno, J.J., Bellucci, G., Patel,
567 M., Allen, M., Altieri, F., Aoki, S., Bolsée, D., Clancy, T., Cloutis, E., Daerden, F., Depiesse, C.,
568 Fedorova, A., Formisano, V., Funke, B., Fussen, D., Garcia-Comas, M., Geminala, A., Gérard,
569 J.C., Gillotay, D., Giuranna, M., Gonzalez-Galindo, F., Ignatiev, N., Kaminski, J., Karatekin, O.,
570 Kasaba, Y., Lefèvre, F., Lewis, S., López-Puertas, M., López-Valverde, M., Mahieux, A., Mason,
571 J., McConnell, J., Mumma, M., Neary, L., Neefs, E., Novak, R., Renotte, E., Robert, S., Sindoni,
572 G., Smith, M., Thomas, I.R., Trokhimovskiy, A., Vander Auwera, J., Villanueva, G., Viscardy, S.,
573 Whiteway, J., Willame, Y., Wilquet, V., Wolff, M., Alonso-Rodrigo, G., Aparicio del Moral, B.,
574 Barzin, P., BenMoussa, A., Berkenbosch, S., Biondi, D., Bonnewijn, S., Candini, G., Clairquin,
575 R., Cubas, J., Delanoye, S., Giordanengo, B., Gissot, S., Gomez, A., Zafra, J.J., Leese, M., Maes,
576 J., Mazy, E., Mazzoli, A., Meseguer, J., Morales, R., Orban, A., Pastor-Morales, M., Perez-
577 Grande, I., Ristic, B., Rodriguez-Gomez, J., Saggin, B., Samain, V., Sanz Andres, A., Sanz, R.,

- 578 Simar, J.F., Thibert, T., NOMAD Team, 2016. Expected performances of the NOMAD/ExoMars
579 instrument. *Planetary and Space Science* 124, 94–104. doi:10.1016/j.pss.2016.03.003.
- 580 Rodgers, C.D., 2000. *Inverse Methods for Atmospheric Sounding: Theory and Practice*. doi:10.
581 1142/3171.
- 582 Sander, S.P., Abbatt, J., Barker, J., Burkholder, J., Friedl, R., Golden, D., Huie, R., Kolb, C.,
583 Kurylo, M., Moortgat, G., Orkin, V., Wine, P., 2011. Chemical kinetics and photochemical data
584 for use in atmospheric studies.
- 585 Serdyuchenko, A., Gorshelev, V., Weber, M., Chehade, W., Burrows, J.P., 2014. High spectral
586 resolution ozone absorption cross-sections - Part 2: Temperature dependence. *Atmospheric Mea-
587 surement Techniques* 7, 625–636. doi:10.5194/amt-7-625-2014.
- 588 Smith, D.E., Zuber, M.T., Solomon, S.C., Phillips, R.J., Head, J.W., Garvin, J.B., Banerdt, W.B.,
589 Muhleman, D.O., Pettengill, G.H., Neumann, G.A., Lemoine, F.G., Abshire, J.B., Aharonson,
590 O., Brown, David, C., Hauck, S.A., Ivanov, A.B., McGovern, P.J., Zwally, H.J., Duxbury, T.C.,
591 1999. The Global Topography of Mars and Implications for Surface Evolution. *Science* 284, 1495.
592 doi:10.1126/science.284.5419.1495.
- 593 Sneep, M., Ubachs, W., 2005. Direct measurement of the Rayleigh scattering cross section in various
594 gases. *Journal of Quantitative Spectroscopy and Radiative Transfer* 92, 293–310. doi:10.1016/
595 j.jqsrt.2004.07.025.
- 596 Spurr, R.J.D., 2006. VLIDORT: A linearized pseudo-spherical vector discrete ordinate radiative
597 transfer code for forward model and retrieval studies in multilayer multiple scattering media.
598 *Journal of Quantitative Spectroscopy and Radiative Transfer* 102, 316–342. doi:10.1016/j.
599 jqsrt.2006.05.005.
- 600 Trompet, L., Mahieux, A., Ristic, B., Robert, S., Wilquet, V., Thomas, I.R., Vandaele, A.C.,
601 Bertaux, J.L., 2016. Improved algorithm for the transmittance estimation of spectra obtained
602 with SOIR/Venus Express. *Applied Optics* 55, 9275. doi:10.1364/AO.55.009275.
- 603 Vandaele, A.C., De Mazière, M., Drummond, R., Mahieux, A., Neefs, E., Wilquet, V., Korablev,
604 O., Fedorova, A., Belyaev, D., Montmessin, F., Bertaux, J.L., 2008. Composition of the Venus

- 605 mesosphere measured by Solar Occultation at Infrared on board Venus Express. *Journal of*
606 *Geophysical Research (Planets)* 113, E00B23. doi:10.1029/2008JE003140.
- 607 Vandaele, A.C., Kruglanski, M., de Mazière, M., 2006. Modeling and Retrieval of Atmospheric
608 Spectra Using ASIMUT, in: *Atmospheric Science Conference*, p. 71.
- 609 Vandaele, A.C., Lopez-Moreno, J.J., Patel, M.R., Bellucci, G., Daerden, F., Ristic, B., Robert,
610 S., Thomas, I.R., Wilquet, V., Allen, M., Alonso-Rodrigo, G., Altieri, F., Aoki, S., Bolsée, D.,
611 Clancy, T., Cloutis, E., Depiesse, C., Drummond, R., Fedorova, A., Formisano, V., Funke, B.,
612 González-Galindo, F., Geminale, A., Gérard, J.C., Giuranna, M., Hetey, L., Ignatiev, N., Kamin-
613 ski, J., Karatekin, O., Kasaba, Y., Leese, M., Lefèvre, F., Lewis, S.R., López-Puertas, M., López-
614 Valverde, M., Mahieux, A., Mason, J., McConnell, J., Mumma, M., Neary, L., Neefs, E., Renotte,
615 E., Rodriguez-Gomez, J., Sindoni, G., Smith, M., Stiepen, A., Trokhimovsky, A., Vander Auwera,
616 J., Villanueva, G., Viscardy, S., Whiteway, J., Willame, Y., Wolff, M., 2018. NOMAD, an Inte-
617 grated Suite of Three Spectrometers for the ExoMars Trace Gas Mission: Technical Description,
618 Science Objectives and Expected Performance. *ssr* 214, 80. doi:10.1007/s11214-018-0517-2.
- 619 Vandaele, A.C., Mahieux, A., Robert, S., Berkenbosch, S., Clairquin, R., Drummond, R., Letocart,
620 V., Neefs, E., Ristic, B., Wilquet, V., Colomer, F., Belyaev, D., Bertaux, J.L., 2013. Improved
621 calibration of SOIR/Venus Express spectra. *Optics Express* 21, 21148. doi:10.1364/OE.21.
622 021148.
- 623 Vandebussche, S., Kochenova, S., Vandaele, A.C., Kumps, N., De Mazière, M., 2013. Retrieval
624 of desert dust aerosol vertical profiles from IASI measurements in the TIR atmospheric window.
625 *Atmospheric Measurement Techniques* 6, 2577–2591. doi:10.5194/amt-6-2577-2013.
- 626 Willame, Y., Vandaele, A.C., Depiesse, C., Lefèvre, F., Letocart, V., Gillotay, D., Montmessin,
627 F., 2017. Retrieving cloud, dust and ozone abundances in the Martian atmosphere using SPI-
628 CAM/UV nadir spectra. *Planetary and Space Science* 142, 9–25. doi:10.1016/j.pss.2017.04.
629 011.

Highlights

- We investigated the impact of gradients along the LOS of a solar occultation experiment
- We focused on the retrieval of ozone using observations acquired by SPICAM/MEx
- We implemented a radiative transfer code (ASIMUT) to take into account gradients
- We used the diurnal variations in the ozone concentration obtained from a GCM (GEM-Mars)
- The impact of gradients on ozone retrievals is strongly related to the GCM model results.